AIAA AVIATION Forum
June 15-19, 2020, VIRTUAL EVENT
AIAA AVIATION 2020 FORUM

10.2514/6.2020-2792

A High-Speed High-Efficiency VTOL Vehicle Using CoFlow Jet Flow Control

Jeremy Boling*, Yan Ren†, Ge-Cheng Zha‡
Department of Mechanical and Aerospace Engineering
University of Miami, Coral Gables, Florida 33124
E-mail: gzha@miami.edu

Cale Zeune§
Aerodynamic Technology Branch,
Aerospace Systems Directorate, AFRL/RQVA
Wright-Patterson AFB, Ohio 45433

This paper conducts a conceptual aerodynamic design and trade study of a CoFlow Jet(CFJ) VTOL (CFJ-VTOL) air vehicle with high speed cruise Mach number of 0.6. The in house high order accuracy FASIP CFD code is used to conduct the full aircraft 3D simulation and wing design trade studies. The vehicle has a tandem wing tailless configuration with the fuselage designed for 1.5 ton payload or 15 passenger seats. The overall aspect ratio of the tandem wing system is 11.65. The CFJ-VTOL concept has both the propeller and wing generating lift at hovering condition to reduce the required power. At cruise, the CFJ is able to enhance the aerodynamic and productivity efficiency due to increased lift and reduced drag at low energy expenditure. A 2D airfoil study is conducted and selects the NACA6415 based CFJ airfoil to form the 3D unswept and untapered wing. A trade study is conducted to configure the tandem wing system, which positions the large wing in the front and the smaller wing with 50% smaller area aft. Such a tandem wings configuration minimizes the front wing tip vortices and downwash interference to the rear wing. At cruise, a very good aerodynamic efficiency $(C_L/C_D)_c$ of 14.6 is achieved with a lift coefficient of 0.812. At hovering static condition, the CFJ wing is positioned at an angle of attack of 80° that keeps the flow attached and generates high lift making use of the flow pulled by the propeller. The CFJ wings generate 19% of the total lift, but consume only 1.5% of the total hovering power. This substantially reduces the disk loading and potentially its associated noise. As a result, the system hovering power is decreased by 21.7%, which reduces the propulsion system weight and benefit the whole mission efficiency. The conceptual aerodynamic design and trade study with high fidelity CFD simulation indicates that the CFJ-VTOL concept is not just feasible to cruise at Mach number 0.6 and higher in transonic regime, it is also possible to increase the mission productivity efficiency substantially (e.g. by 100% or higher) compared to the State of the Art conventional VTOL aircraft.

*Ph.D. Candidate
†Postdoc Researcher, Ph.D., AIAA member
‡Professor, AIAA Associate Fellow
§Chief Engineer

Nomenclature

V	Flow Velocity
ρ	Air Density
α, AoA	Angle of Attack
$\dot{m}$	Mass Flow Rate
M	Mach Number
M_i	Isentropic Mach Number
Re	Reynolds Number
L	Aerodynamics Lift
D	Aerodynamic Drag
p	Static Pressure
p_0	Total Pressure
η	Pumping Power
q_∞	Freestream Dynamic Head, $\frac{1}{2}\rho_\infty {V_\infty}^2$
C_L	Lift Coefficient, $\frac{L}{q_\infty S}$
C_D	Drag Coefficient, $\frac{D}{q_\infty S}$
C_M	Moment Coefficient, $\frac{M}{q_\infty S c}$
C_p	Pressure Coefficient, $\frac{p-p_\infty}{q_\infty}$
C_μ	Jet Momentum Coefficient, $\frac{\dot{m}_j v_j}{q_\infty S}$
$(\frac{L}{D})$	Conventional Aerodynamic Efficiency
P_c	CFJ Power Coefficient, $\frac{P}{q_\infty S V_\infty}$
$(\frac{L}{D})_c$	Corrected Aerodynamic Efficiency for CFJ Airfoil, $\frac{L}{D+P/V_\infty} = \frac{C_L}{C_D+P_c}$
$(\frac{C_L^2}{C_D})$	Productivity Efficiency Coefficient
$(\frac{C_L^2}{C_D})_c$	Corrected Productivity Efficiency Coefficient for CFJ Airfoil
∞	Free Stream Conditions
j	Jet conditions
$i_{wf}, i_{wa},$	flow incidence angle of the front wing and aft wing
P_P	Propeller actuator power coefficient $\frac{2}{\rho V_\infty^3 S}\sqrt{\frac{F^3}{2\rho A}}$
P_L	Power loading, power/lift
D_L	Disk loading, thrust of the actuator disk/actuator disk area
P_{Lc}	Power loading coefficient
D_{Lc}	Disk loading coefficient

I. Introduction

VTOL utility aircraft still mostly cruise at subsonic Mach number below 0.42 including the V-280 and SB-1 from the Future Vertical Lift (FVL) program as shown in Table 1. The FVL program does increase the cruise speed compared with V-22, but only modestly. The barrier in increasing VTOL aircraft cruise speed is largely attributed to low efficiency. For V-22 and V-280, the radius of the rotor disk is nearly as long as half of the wing span. Such large rotor disks limit the cruise speed to obtain efficient propellers. SB-1 is a helicopter with two counter rotating propellers. Since helicopter propellers primarily generate the flow momentum in the vertical direction, it is difficult to make a helicopter configuration to cruise forward at a high Mach number and still keep a good aerodynamic efficiency. It is outstanding that the SB-1 cruises at Mach 0.37, even slightly faster than V-22, but it may be close to its limit as a helicopter.

Table 1. Cruise Mach number comparison of the VTOL aircraft

Performance /Vehicle	V-22	V-280	SB-1	CFJ-VTOL
Mach	0.36	0.42	0.37	0.6

Recently, the development for on-demand-mobility(ODM) electric VTOL (eVTOL) aircraft for urban transportation has shed some new light on VTOL aircraft design, specifically, using fixed wing configurations with distributed electric propulsion (DEP) . The DEP for eVTOL mostly uses multiple small

propellers or ducted fans along the fixed wings. The small propellers are intended to have higher efficiency and lower noise than the large rotor blades of conventional helicopters. DEP has great potential to provide several crucial advantages,[1,2] including lower noise, faster cruise speed, higher cruise efficiency, higher safety due to high propulsion system redundancy, higher stability, easier operation, higher passenger comfort, lower cost for manufacturing and operation, and being fully autonomous.

All the current VTOL aircraft including the DEP systems utilize propellers to generate hovering vertical lift by articulating the propellers vertically, or by rotating the wings with propellers to vertical lifting direction, or by dedicated propellers used for hovering only. The special requirement for hovering is in conflict with high cruise efficiency. For example, the dedicated propellers for hovering are not used for cruise. To reduce the cruise drag, their blades are usually aligned with the struts. Even so, the whole hovering structure serves to significantly increase the cruise drag. Furthermore, all these technologies use direct vertical lifting(DVL) from propellers, which requires that the propeller hovering lift must be greater than the aircraft weight. The power requirement for hovering is very high when compared to cruise. This also means higher propeller disk loading and associated noise. The high hovering power requires larger and heavier propulsion systems, which penalize the whole mission efficiency.

Compared with the DVL using "brute" lifting force, the conventional takeoff/landing (CTOL) aircraft using runways is much more energy efficient and quiet because the required thrust is only a fraction of the aircraft weight, e.g., 20%. The reason is that CTOL relies on the lift generated by the wings with the dynamic pressure from the free stream. The power and energy consumption is much smaller than VTOL aircraft. In addition, the noise level of CTOL is also substantially lower due to low propeller disk loading.

Because VTOL aircraft all have large disparity for the aerodynamic requirements between hovering and cruise, they suffer significantly lower system efficiency than CTOL aircraft due to two factors: 1) low Figure of Merit at VTOL hovering; 2) low cruise lift to drag ratio. Fig. 1 and 2 adopted from the AHS and NARI report of 2018[3] present the system efficiency of the state of the art (SoA) VTOL aircraft, which contain almost all the existing VTOL aircraft including helicopter and the recent fixed wing ODM eVTOL for urban transportation. Fig. 1 indicates that the maximum hovering figure of merit (FM) is less than 0.65. FM represents the hovering efficiency. Fig. 2 indicates that the tilt rotorcraft(e.g. V22) has maximum L/D of 8.3, substantially higher than 5.3 for helicopter. The recent development of fixed wing ODM eVTOL is able to push the maximum L/D to 9.

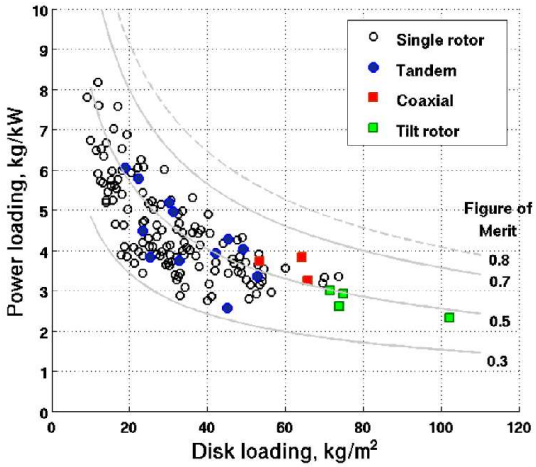

Figure 1. SoA VTOL power loading vs disk loading and Figure of Merit, plot adopted from.[3]

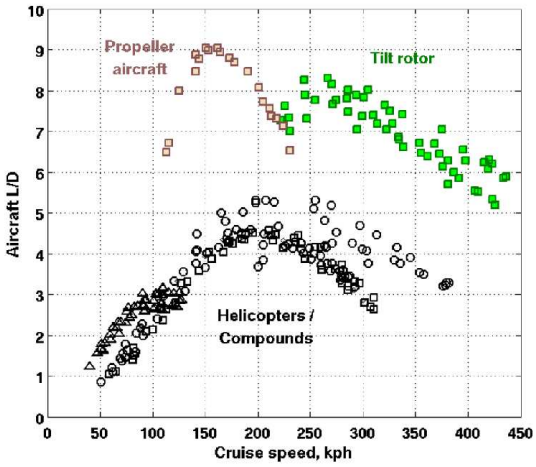

Figure 2. SoA VTOL cruise lift to drag ratio, plot adopted from.[3]

It is appealing if VTOL aircraft can combine the advantages of conventional VTOL DVL and CTOL to generate lift from the wings and propellers. Such technology would have great potential to dramatically increase the system efficiency and flight speed. The recent co-flow jet (CFJ) -VTOL (CFJ-VTOL) concept suggested by Zha et al[4] provides such a possibility. The purpose of this paper is to conduct a conceptual aerodynamic design of a high speed and high efficiency VTOL vehicle using the CFJ-VTOL concept at Mach number of 0.6. For high speed VTOL aircraft, the mission design and aircraft sizing must be conducted simultaneously for both the hovering and cruise phase to consider the whole flight envelop. As indicated by Table 1, the cruise Mach number of 0.6 is 43% faster than the state of the art. The goal is not just to achieve a high cruise speed, but also to achieve high mission efficiency. The target is to achieve an improvement of the mission productivity efficiency by 100% or more.

I.A. CoFlow Jet (CFJ) Airfoil

The coflow jet (CFJ) active flow control airfoil concept developed by Zha and his team is described in a series of publications.[4–30] The CFJ airfoil has an injection slot near the leading edge(LE) and a suction slot near the trailing edge(TE) on the airfoil suction surface. A small amount of mass flow is withdrawn into the interior of the airfoil near the TE, pressurized and energized by a micro-compressor actuator inside the airfoil, and then injected near the LE in the direction tangent to the main flow. The whole process does not add any mass flow to the system and hence is a zero-net mass-flux flow control. The CFJ airfoil has very low energy expenditure, because the jet is injected at the leading edge peak suction location, where the main flow pressure is near the lowest and it hence requires a low power to eject the flow, and it is sucked at the trailing edge, where the main flow pressure is near the highest and it hence requires a low power for the flow to be sucked into the airfoil. The low energy expenditure is the key factor enabling the CFJ wing not only to achieve ultra-high lift coefficients, but also to obtain very high productivity efficiency at cruise when the flow is benign at low angle of attack.[14,28,29,31]

The drag reduction mechanism of CFJ airfoil is to create a super-suction effect at the leading edge with very low pressure caused by the injection jet induction effect, which reduces the pressure drag. The surface friction drag may not be reduced since the flow tends to be turbulent triggered by the injection jet near airfoil leading edge. Surface friction drag reduction has a lower limit that the entire wing surface has laminar flow, which is very difficult if not impossible to achieve. The lower limit of pressure drag is when a vacuum occurs at the leading edge. This gives a much larger room for drag reduction, so large that a high thrust can be generated by CFJ only.[7,8,12] A CFJ wing is hence naturally a distributed propulsion system. Yang and Zha[17] discovered in 2017 that a CFJ airfoil can achieve Super-Lift Coefficient(SLC), which exceeds the theoretical limit of potential flow developed by Smith.[32] Overall, CFJ active flow control is demonstrated to have very high effectiveness for lift enhancement, drag reduction and stall angle of attack increase at low energy expenditure. Its radical performance fosters new concept of aircraft systems.

II. CFJ-VTOL Aircraft Concept

The CFJ-VTOL concept was suggested by Zha et al in 2019.[4] It is to utilize the advanced CFJ airfoil with propellers to generate substantial hovering lift from the CFJ wings instead of from the propellers only. The CFJ airfoil can sustain very high angle of attack[17,18] with ultra-high lift coefficient and is virtually stall free. However, at static hovering condition, the CFJ airfoil itself will not generate high lift unless there is freestream flowing toward the airfoil.

The CFJ-VTOL concept[4] is depicted in Fig. 3 and 4, which has propellers mounted on the upper surface of a CFJ wing. The propeller does not completely face upward as conventional VTOL aircraft that rely on the propellers to generate all the lift. The propeller of CFJ-VTOL faces upward and forward as shown in Fig. 4. It generates a partial lift for the VTOL system and induces freestream to the CFJ airfoil at static hovering condition. Enhanced by the freestream, the CFJ airfoil at a very high angle of attack(e.g. 80°) will generate a ultra-high lift coefficient at a much lower power consumption than the propellers. To overcome the gross weight of a airplane, the propeller disk loading will be significantly lower than typical VTOL aircraft since it is not required to be the sole generator of vertical lift. The low propeller disk loading will decrease the power loading, increase the hovering FM, and reduce the VTOL noise level. In addition, the propeller noise radiating to the ground will be substantially shielded by the wing surfaces.

The propeller position located downstream of the CFJ injection slot has a very important advantage to enhance the overall CFJ-VTOL efficiency. The propeller has a suction effect on the flow and reduces the power required for the CFJ to achieve a certain lift coefficient. Such a position is optimized to significantly benefit the hovering efficiency as shown in Fig. 3 as well as the cruise efficiency.

II.A. VTOL and ESTOL in One System[4]

The same proposed CFJ-VTOL system can be used for extremely short takeoff/landing(ESTOL) aircraft. The resultant force coefficient F_C of the propeller-CFJ airfoil system illustrated in Fig. 4 has the following relation:

$$F_C = F(\alpha, \beta, V_\infty, P_C, P_P) \tag{1}$$

where α is the angle between the CFJ airfoil chord and the horizontal direction, β the angle between the airfoil chord and the propeller disk, P_C the power coefficient of CFJ defined in Eq. (7), P_P the power

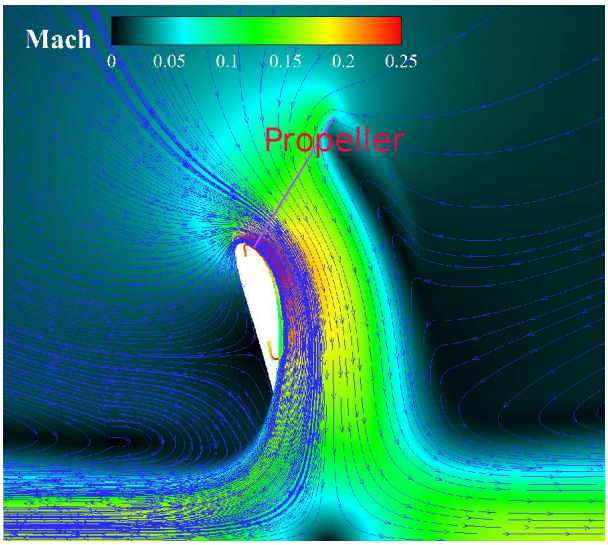

Figure 3. Zoomed in Mach contours of the CFJ airfoil with a propeller for VTOL.

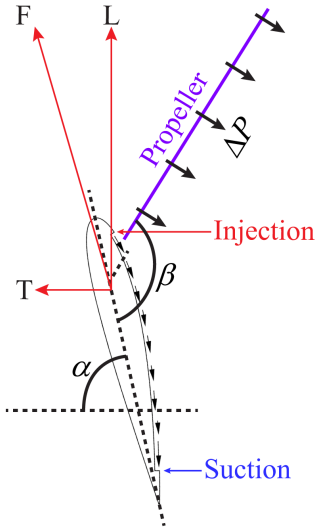

Figure 4. Sketch of a CFJ-V/STOL concept.

coefficient of the propeller actuator defined in Eq. (22). In general, increasing $\alpha, \beta,\ P_C,\ P_P$ will increase F_C provided the flow is remained attached. At the static condition with $V_\infty = 0$, if $\beta,\ P_C,\ P_P$ are fixed, the magnitude of F_C is constant and the direction is only determined by α. In the CFJ-VTOL concept, the α is 80° and the flow remains attached with a large lift coefficient generated from the CFJ wing.

At the static condition with an α controlled to generate the resultant force pointing vertically upward, the system is configured for VTOL. When the α is decreased from the VTOL angle, the resultant force will point forward and upward for ESTOL with a thrust component. In other words, the same propeller-CFJ wing system can be used for both VTOL and ESTOL by controlling the CFJ wing chord angle α. The ESTOL will substantially decrease the power consumption compared to the VTOL as demonstrated in.[4] This provides versatile features for an air vehicle. When there is no space for a run way, the vehicle can choose VTOL mode. When there is a small space which can be used as a runway, the air vehicle can choose ESTOL mode to save energy.

II.B. The Proposed High Speed VTOL Air Vehicle

Fig. 5 shows the proposed CFJ-VTOL vehicle, which uses a tandem wing configuration with no vertical tail. The advantages of tandem wing configuration include: 1) generating lift from two lifting vectors for hovering with high stability; 2) high structure strength and high aircraft maneuverability; 3) overcoming the increased pitching moment coefficient of CFJ wings caused by high lift; 4) more compact size. But the tandem wings suffer some aerodynamic efficiency loss due to reduced aspect ratio and wing-wing interference.

Fig. 5 on the left shows the vehicle at hovering mode with the wing tilted to 80° as in Fig. 3. At cruise, the wing is tilted to horizontal as shown on the right in Fig. 5. The tailless flight control concept is to use different coflow jet and propeller strength along the span to create unbalanced lift and thrust (or drag) to generate the rolling moment, yaw moment, and pitching moment with the tandem wings; this remains to be worked out, but should be feasible. The CFJ and propeller strengths will be controlled at different span locations by the micro-compressor power and propeller motor power, e.g. RPM.

The wing planform area is sized to cruise at Mach 0.6 at the altitude of 41,000 ft with a payload of 1500 kg. The aspect ratio of the tandem wing system is 18.7 considering the fuselage width as a part of the wing span. The maximum wing span is 13.57 m and the total wing area is 12 m^2. A series of propellers are installed downstream of the CFJ injection (see Fig. 3 and 4) to form a distributed propulsors with the CFJ micro-compressors embedded inside the wing. The diameter of the propellers is equal to the wing chord to enable the high speed cruise with low tip speed to have high efficiency. This makes the propeller actuator disk size area the same as the wing area. This paper is focused on the aerodynamic design and analysis of the hovering and cruise. The mission performance will not be presented to save the space.

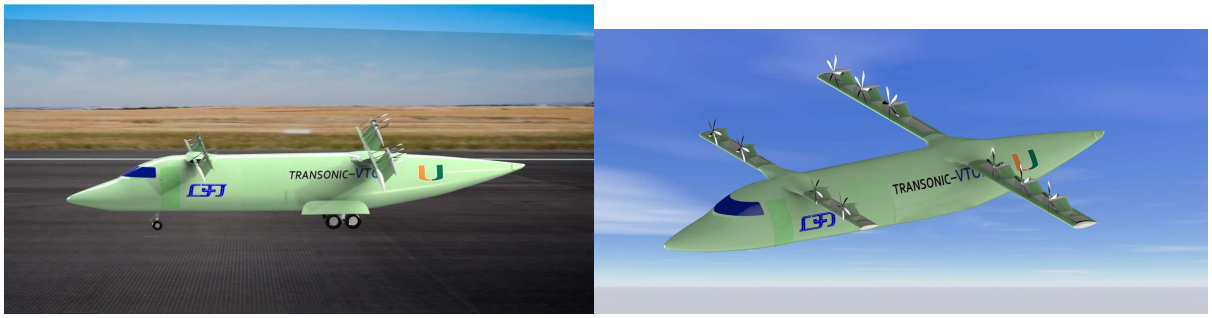

Figure 5. High speed CFJ VTOL from takeoff to cruise

II.C. Aerodynamic Parameters

The parameters used to define the CFJ tandem wing system are described in this section.

The injection jet momentum coefficient C_μ is used to describe the CFJ strength as:

$$C_\mu = \frac{\dot{m}V_j}{\frac{1}{2}\rho_\infty {V_\infty}^2 S} \tag{2}$$

where $\dot{m}$ is the injection mass flow, V_j is the mass-averaged injection velocity, ρ_∞ and V_∞ denote the free stream density and velocity, and S is the airfoil planform area.

The conventional airfoil aerodynamic efficiency is defined as

$$(\frac{L}{D}) = \frac{C_L}{C_D} \tag{3}$$

For CFJ wing, the ratio above represents the pure aerodynamic relationship between lift and drag. Taking into account the energy consumption of the CFJ, the conventional aerodynamic efficiency is modified by converting the power consumption into a corresponding drag force. The equation of the corrected aerodynamic efficiency is given as the following[12]

$$(\frac{L}{D})_c = \frac{L}{D + \frac{P}{V_\infty}} \tag{4}$$

in which the CFJ pumping power consumption P is converted into a force $\frac{P}{V_\infty}$ added to the aerodynamic drag D. The formulation above can be further expressed using the non-dimensional coefficients C_L, C_D and P_c as

$$(\frac{C_L}{C_D})_c = \frac{C_L}{C_D + P_c} \tag{5}$$

Note that when the pumping power is set to 0, $(\frac{L}{D})_c$ returns to conventional aerodynamic efficiency definition. The C_L and C_D calculation needs to include the CFJ reactionary force as described by Zha et al.[5]

The CFJ power required is determined by the total enthalpy rise from the suction duct outlet to the injection duct inlet.[12] The total enthalpy rise can be achieved by the embedded micro-compressors. The power required by the CFJ (P) can be expressed as:

$$P = \frac{\dot{m}H_{t2}}{\eta}(\Gamma^{\frac{\gamma-1}{\gamma}} - 1) \tag{6}$$

where γ is the specific heat ratio, Γ the total pressure ratio of the micro-compressor, H_{t2} the total enthalpy at the compressor inlet, $\dot{m}$ the jet mass flow rate, η the micro-compressor efficiency and is taken at 100% to compute the required power.

Eq. (6) indicates that the power required for CFJ is linearly determined by the mass flow rate and exponentially by the total pressure ratio. This relationship in fact applies to all the active flow controls based on fluidic actuators. Thus, C_μ should not be used to represent the power consumption of active flow control.[12,28] For example, a high C_μ could have a substantially lower power consumption than a smaller C_μ if the high C_μ is created by a large mass flow rate and low jet velocity, which needs a significantly lower

total pressure ratio.[28,29] Yang and Zha[17] find that the only parameter correlated well with the maximum lift coefficient of CFJ airfoil is the power coefficient defined below:

$$P_c = \frac{P}{\frac{1}{2}\rho_\infty V_\infty^3 S} \tag{7}$$

where P is the CFJ required power defined in Eq. 6.

The transportation capability of an airplane is measured by how much total weight the aircraft can move for the maximum distance. In Yang et. al (2017),[17] a term "productivity" is defined as the product of the total weight by the maximum range to represent the transportation capability of an airplane.

For a jet engine airplane, the total weight of the aircraft decreases during flight. A non-dimensional productivity parameter is hence defined using the aircraft averaged weight as below:

$$C_{RW} = \frac{R\overline{W}}{\frac{1}{2c_t}\bar{\rho}V_\infty^3 S} = \frac{C_L^2}{C_D}\ln\frac{W_0}{W_f} \tag{8}$$

where R is the aircraft range, $\overline{W}$ is the averaged weight of the aircraft during cruise, c_t is the engine cruise thrust specific fuel consumption[fuel weight(N)/(thrust(N) s)], $\bar{\rho}$ is the averaged air density during cruise due to altitude variation, S is the wing platform area, W_0 is the aircraft initial gross weight at takeoff, W_f is the final weight at landing. This formulation is obtained from the Breguet Range Equation. The productivity parameter represents the productivity of the aircraft with the fuel consumed per unit time.

For a full electric battery powered propeller airplane, the aircraft weight will not change during flight. The productivity parameter is defined as:

$$C_{RW} = \frac{RW}{\frac{1}{2}\rho V_\infty^2 S E_c/g} = \eta\frac{C_L^2}{C_D}\frac{W_b}{W_0} \tag{9}$$

where E_c is the battery specific energy density (Wh/kg), W_b is the total battery weight, W_0 is the gross weight, η is the propulsion system efficiency (e.g. propeller).

Clearly, both Eq. (8) and (9) indicate that the productivity parameter is determined by C_L^2/C_D, which is thus defined as productivity efficiency. The productivity efficiency is considered as a more comprehensive parameter than the conventional aerodynamic efficiency C_L/C_D to measure the merit of an airplane aerodynamic design for cruise performance. The former includes not only the information of C_L/C_D, but also the information of the aircraft weight represented by C_L.

For CFJ airfoil, the productivity efficiency should also include the CFJ power consumption and is defined as below:

$$\frac{C_L^2}{C_{Dc}} = \frac{C_L^2}{C_D + P_C} \tag{10}$$

This study involves a tandem wing configuration. For example, the coefficient of lift for each wing can be defined individually as:

$$C_{L1} = \frac{L_1}{\frac{1}{2}\rho_\infty {V_\infty}^2 S_1}, \quad C_{L2} = \frac{L_2}{\frac{1}{2}\rho_\infty {V_\infty}^2 S_2}, \tag{11}$$

where the subscript 1 and 2 stand for the first and second wing. For the aircraft system with tandem wings, the system lift coefficient is defined as the total lift based on the total wing area below:

$$C_{Lt} = \frac{L_1 + L_2}{\frac{1}{2}\rho_\infty {V_\infty}^2 (S_1 + S_2)} \tag{12}$$

where the subscript t stands for tandem wing.

Substituting Eq. (11(to Eq. (12), the system lift coefficient can be expressed as:

$$C_{Lt} = \frac{C_{L1}S_1 + C_{L2}S_2}{S_1 + S_2} \tag{13}$$

Eq. (13) is actually the same as the area weighted lift coefficient. Similarly, the coefficient of system drag and CFJ power can be defined as:

$$C_{Dt} = \frac{C_{D1}S_1 + C_{D2}S_2}{S_1 + S_2} \tag{14}$$

$$P_{ct} = \frac{P_{c1}S_1 + P_{c2}S_2}{S_1 + S_2} \tag{15}$$

The corrected drag coefficient is:

$$(C_{Dc})_t = C_{Dt} + P_{ct} \tag{16}$$

The aerodynamic efficiency and the productivity efficiency of the tandem wing system then can be defined following the same way as Eq. (5) and Eq. (10). To see the relations clearly, we take the aerodynamic efficiency of the tandem wing as an example below:

$$\begin{aligned}(\frac{L}{D_c})_t &= \frac{L_1 + L_2}{D_1 + D_2 + P_1/V_\infty + P_2/V_\infty} = \frac{C_{Lt}\frac{1}{2}\rho_\infty {V_\infty}^2(S_1 + S_2)}{C_{Dt}\frac{1}{2}\rho_\infty {V_\infty}^2(S_1 + S_2) + P_{ct}\frac{1}{2}\rho_\infty {V_\infty}^2(S_1 + S_2)} \\ &= \frac{S_1C_{L1} + S_2C_{L2}}{S_1C_{D1} + S_2C_{D2} + S_1P_{c1} + S_2P_{c2}}\end{aligned} \tag{17}$$

That is:

$$(\frac{L}{D_c})_t = \frac{C_{Lt}}{(C_{Dc})_t} \tag{18}$$

Propeller disk loading (D_L) and power loading (P_L) are used to describe the performance of VTOL hovering and are defined as:

$$D_L = L/A, \quad P_L = P/L \tag{19}$$

where L is the lift generated by the propeller, A is the propeller disk area, P is the propeller required power to generate the lift, L. Power loading describes the power required per unit lift.

The disk loading coefficient is:

$$D_{L_c} = \frac{L/(1/2\rho V^2 S)}{A/S} = \frac{C_L}{A_c} = \frac{D_L}{\frac{1}{2}\rho V_\infty^2} \tag{20}$$

Where $A_c = A/S$, and A is the disk area and S is the wing planform area. The power loading coefficient is:

$$P_{L_c} = \frac{P/(1/2\rho V^3 S)}{L/(1/2\rho V^2 S} = \frac{P_p}{C_L} = \frac{P_L}{V_\infty} \tag{21}$$

The power coefficient for the propeller actuator is:

$$P_P = \frac{2}{\rho V_\infty^3 S}\sqrt{\frac{F^3}{2\rho A}} \tag{22}$$

where F is the total force produced by the propeller actuator normal to the propeller disk.

During hovering, the following relations apply based on 1D actuator disk theory:

$$P_L = \sqrt{D_L\frac{1}{2\rho}} \tag{23}$$

$$P_{L_c} = \frac{\sqrt{D_{L_c}}}{2} \tag{24}$$

For a CFJ-VTOL system, the lift will be generated by both the propeller and the wing. Thus the power loading can be used for the whole system or for each component such as the propeller or the wing.
For the system,

$$P_{L_{CFJ-VTOL}} = \frac{P_{CFJ} + P_{actuator}}{L_{CFJ} + L_{actuator}} \tag{25}$$

For the component,

$$P_{L_{CFJ}} = \frac{P_{CFJ}}{L_{CFJ}} \tag{26}$$

$$P_{L_{actuator}} = \frac{P_{actuator}}{L_{actuator}} \tag{27}$$

II.D. Numerical Approach

The in-house high-order-accuracy CFD code FASIP (Flow-Acoustics-Structure Interaction Package)[33–35,35–43] is used for the CFD simulation in this paper. FASIP solves the full 3D time dependent Navier-Stokes equations in generalized coordinates using structured mesh that can treat complex geometries. The high-order shock-capturing schemes, including 3rd order MUSCL scheme,[44] 3rd, 5th and 7th order WENO schemes and a finite compact scheme combining a shock detector and 6th order Padé compact scheme, are utilized in the code.[36–40] A set of 4th order and 6th order central differencing schemes are devised to match the same stencil width of the WENO schemes for the viscous terms.[34,35] The inviscid fluxes are calculated by a low diffusion E-CUSP(LDE) scheme suggested by Zha et al[40] or by the Roe scheme.[?] An implicit 2nd order time-accurate scheme with pseudo time and unfactored Gauss-Seidel line relaxation is employed for time marching. The turbulence modeling in the code include Reynolds averaged Navier-Stokes(RANS), Delayed Detached Eddy Simulation(DDES),[45,46] Improved DDES(IDDES),[26] large eddy simulation(LES).[35,42] The propeller is simulated using an actuator disk BC, across which the static pressure is increased by a percentage ΔP based on the local static pressure upstream of the disk. Even though the pressure increase percentage is uniform across the dick, the pressure increase is not because of the non-uniform local static pressure upstream of the disk. The pressure jump across the disk is handled by the approximate Riemann solver in the FASIP code similar to a shock wave. The MPI parallel computing is implemented and a high scalability is achieved.[41] The code is validated with the DLR-F6 wing/body configuration and accurately predict the lift, drag and moment coefficient.[47] The code is extensively validated with CFJ airfoil flows.[9,12,16,41,42,46]

II.E. Boundary Conditions

For the 3D hovering static case, a slice of the mesh is shown in Fig. 6. The far field extends 250 chord lengths away radially, and 45 chord lengths in the spanwise direction. The wing is one chord above ground to mimic the hovering ground effect. The total mesh size for 3D tandem wing hovering is 10.5 million, split into 249 blocks. For the hovering static condition, the freestream conditions have zero velocity, which cannot be used to normalize the aerodynamic forces. Therefore, a freestream reference Mach number of 0.04 is used to normalize the aerodynamic forces. This results in $V_\infty = 13.9m/s$, $\rho_\infty = 1.23$, which is used to calculate the dynamic pressure. The 3D tandem wing study without fuselage has a mesh size of 10.6 million. The CFD solver used for the 3D hovering is unsteady IDDES.

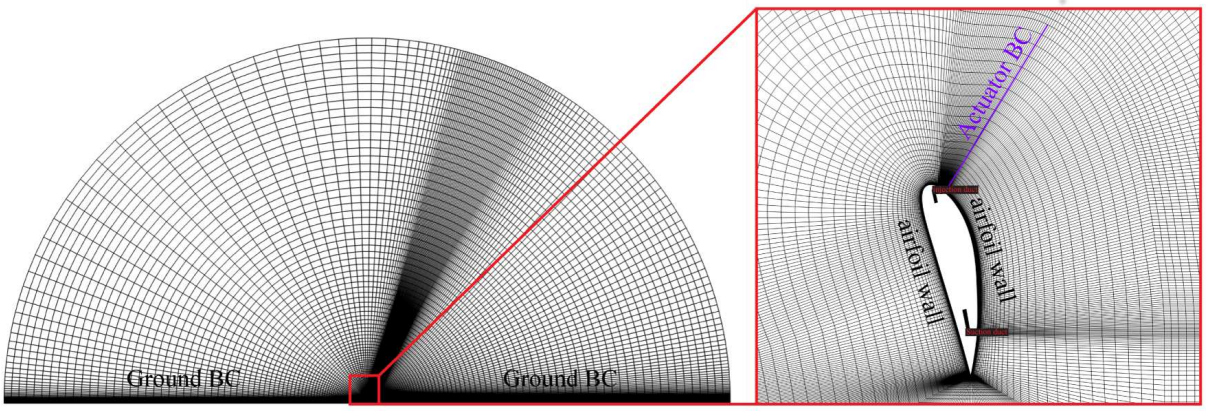

Figure 6. A slice of the computational mesh used for hovering condition with ground.

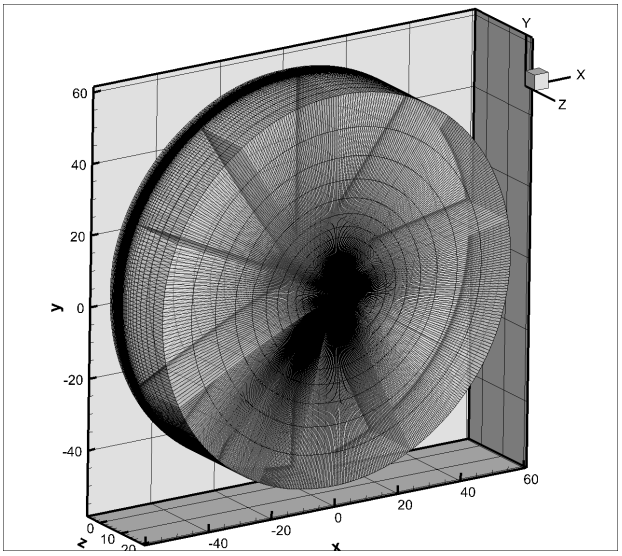

Figure 7. 3D CFD mesh and farfield domain.

For the 3D cruise simulation for single wing and tandem wing without fuselage, the freestream Mach number is 0.6 and the Reynolds number based on the wing chord is 5.35×10^6. The computational domain has O-mesh topology as shown in Fig. 7 and the radial far-field boundary located 55 chord lengths. The spanwise far-field is located 20 chord away from the wing tip. Total pressure, total temperature and flow angles are specified at the injection duct inlet, as well as the upstream portion of the far field. Constant static pressure is applied at the suction duct outlet as well as the downstream portion of the far field. Symmetry boundary conditions are applied at the root of the wing. The CFJ ducts are meshed using "H" topology while the domains around the airfoil are meshed using "O" topology. The total mesh size is 7.8 million cells, split into 139 blocks for parallel computation. The first grid point on the wing surface is placed at y+ = 1. The radial far field is 30 chord lengths. In the span-wise direction, the far-field extends 25 chord lengths. The simulation of the cruise conditions employs the 3D steady state RANS solver with S-A one equation turbulence model.

The propeller is modeled by a rectangle actuator disk BC to mimic the distributed propulsors along the wing as shown in Fig. 5, across which the static pressure is increased by a percentage ΔP based on the local static pressure upstream of the disk. The rectangular actuator disk also allows consistent mesh topology between 2D and 3D cases.

Table 2 lists the computed cases, CFD Mesh size and number of mesh blocks, farfield boundary size, and Navier-Stokes Solver. For all the steady state, unsteady, and IDDES N-S solvers, the numerical schemes used are the 3rd order WENO scheme with the LDE scheme of Zha et al[40] for inviscid fluxes and 2nd order central differencing for the viscous terms. The turbulence model is the one equation S-A model for RANS and URANS. All the simulated cases have the propellers included even though some results may not show them.

Table 2. Computed cases, CFD Mesh, farfield boundary size, and Navier-Stokes Solver

Case	Mesh Size	Far-Field Boundary	Mesh Blocks	N-S Solver
2D Single Wing, Hovering	92,714	250C radially	23	URANS
3D Tandem Wing, Hovering	10,520,400	250C radial, 50C spanwise	249	IDDES
2D Single Wing, Cruise	78,417	100C radial	31	RANS
3D Single Wing, Cruise	7,435,680	50C radial, 30C spanwise	149	RANS
3D Tandem Wing, Cruise	10,145,280	50C radial, 30C spanwise	183	RANS
3D Full Aircraft, Cruise	14,420,960	70C radial, 100C inlet and outlet	288	RANS

III. Results and Discussions

As shown in Table 2, extensive cases are simulated for the design trade studies for 2D single CFJ airfoil at hovering and cruise condition, 3D single CFJ wing with aspect ratio of 10 at hovering and cruise condition, tandem wing with aspect ratio of 11.65 at hovering and cruise condition, and the full aircraft with fuselage and tandem wing with aspect ratio of 11.65 for cruise condition. Only the most relevant results on the 2D airfoil selection, 3D tandem wing design and the full aircraft simulation are reported to save space.

III.A. 2D Airfoil Selection

The first essential task for this high speed CFJ-VTOL design is to determine the airfoil. Since the cruise Mach number is 0.6 and the flow on the airfoil is in the transonic regime. A first consideration is a transonic supercritical airfoil, NASA-SC(2) 0714, which is demonstrated to have excellent low speed performance achieving super-lift coefficient.[48] It performs very well for the CFJ-VTOL configuration at static hovering condition. However, a problem appears at the cruise condition. Figure 8 on the left shows the flow condition of the CFJ-VTOL system with the CFJ-NASA SC(2) 0714 supercritical airfoil at cruise Mach number of 0.6. Due to the large leading edge radius, the flow reaches supersonic immediately downstream of the leading edge. This makes the propeller to be located in supersonic flow as shown in Figure 8, which significantly decreases the system aerodynamic efficiency. The propeller position at downstream of the CFJ injection is desirable under hovering condition to minimize the hovering power. One solution to place the propeller at the subsonic freestream is to move the propeller to upstream of the airfoil. Such a system to move the propeller will increase the system complexity and weight. The ideal configuration is to use a fixed propeller location for both hovering and cruise.

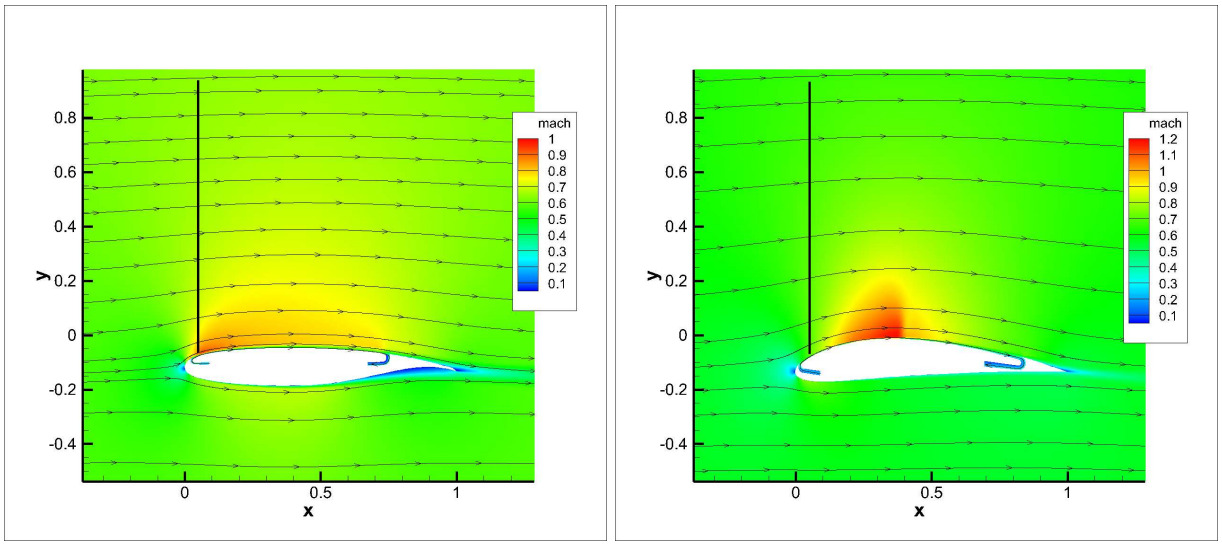

Figure 8. Mach contours at cruise; Left: CFJ-NASA SC(2) 0714 airfoil; Right: CFJ-NACA-6415 airfoil

A simple method to avoid moving the propeller is to use a subsonic airfoil that has a high camber with the supersonic region located in the mid-chord area instead of immediately downstream of the leading edge. Figure 8 on the right shows the simulation results of CFJ-NACA -6415 subsonic airfoil at cruise Mach 0.6 and at angle of attack (AoA) of 0°. The propeller is located at a fairly uniform subsonic flow location with the supersonic flow downstream of the propeller. The CFJ-NACA 6415 airfoil hence allows the propeller installed at the hovering position downstream of the CFJ injection slot, which maximizes both the hovering and cruise efficiency. The 2D CFJ-NACA-6415 airfoil achieves excellent cruise efficiency at Mach 0.6 with C_L/C_D of 123.8 and $C_L/(C_D)_c$ of 76.24. The CFJ-NACA -6415 airfoil also performs excellently at static hovering condition. The final selected airfoil is hence the CFJ-NACA -6415 airfoil.

III.B. Tandem Wing Study

A design issue with tandem wing is that the two wings need to be considered as a system to maximize the efficiency. For example, the front wing's wake and tip vortex may affect the rear wing. The relative

position of the front wing and rear wing is very important, including the horizontal and vertical distances between the two wings, the size of the wings, etc. The total wing area is $12m^2$ and is split to the two wings in this study with the large wing area being twice of the size of the small wing. The area ratio of 2:1 is somewhat arbitrary to have one wing span substantially longer than the other to avoid the tip vortex. It is by no means optimized. A separated trade study of the wing area ratio is ongoing. The wing chord is the same, which makes the large wing have an aspect ratio (AR) of 14 and the small wing have an AR of 7. The overall, combined wing aspect ratio is 11.65. Both wings are straight with no sweep and taper. For simulation efficiency and simplicity, the tandem wing study does not include the aircraft fuselage. A symmetric boundary conditions is applied at the wing root and a zero gradient boundary condition is used in the span-wise far field boundary. The wing tips are resolved with refined mesh and no slip wall boundary condition.

III.B.1. Front Wing AR7, Rear Wing AR14

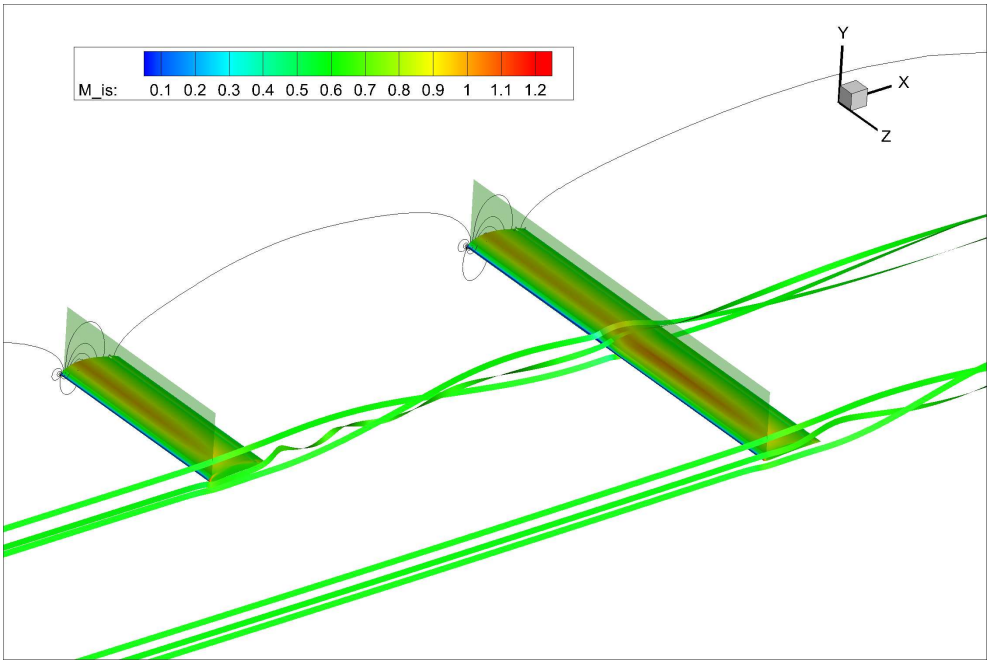

Figure 9. Tandem Wing Mach contours and streamlines, front wing: AR7, $i_{wf} = 0°$; rear wing: AR14, $i_{wa} = 0°$

Figure 9 shows the initial tandem wing configuration with the small wing in the front and the large wing in the back with the two wings at the same level. The front wing's tip vortex directly strikes the rear wing. The translucent box in Figure 9 is the propeller actuator disk. The horizontal distance between the wings is 7 chord lengths. The actuator strength ΔP of 0.4% is used based on the 2D cruise configuration, which is sufficient to overcome the drag of the wings and the fuselage to be added.

Figure 10 shows the total pressure contours of the initial tandem wing configuration at the inner span section. The boundary layer wake of the front wing goes beneath the rear wing even though they are at the same level. This is because the first wing's wake has the tendency to descend due to the wing lift circulation and downwash. The propellers (actuator disc) energize the flow and generate a total pressure jump for each propeller as shown in the contours. The rear wing downstream is inside the front wing's energized propeller wake.

The trade study to optimize the distance between the two wings translates the rear wing both vertically and horizontally. Some incidence angle study is attempted, but based on 2D results, there is not much room for improvement above an incidence angle of 0°. Figure 11 shows Mach contours of the tandem wing configuration with the rear wing translated vertically up and down by one chord as an example.

Figure 12 presents the corrected aerodynamic efficiency, productivity efficiency and lift coefficient of the initial tandem wing configuration when the rear wing is translated vertically. The larger wing contributes more to each overall quantity as the total system is weighted by the area of each wing. Fig. 12 indicates that the tandem wing system has the lowest efficiency when the two wings are aligned at the same level.

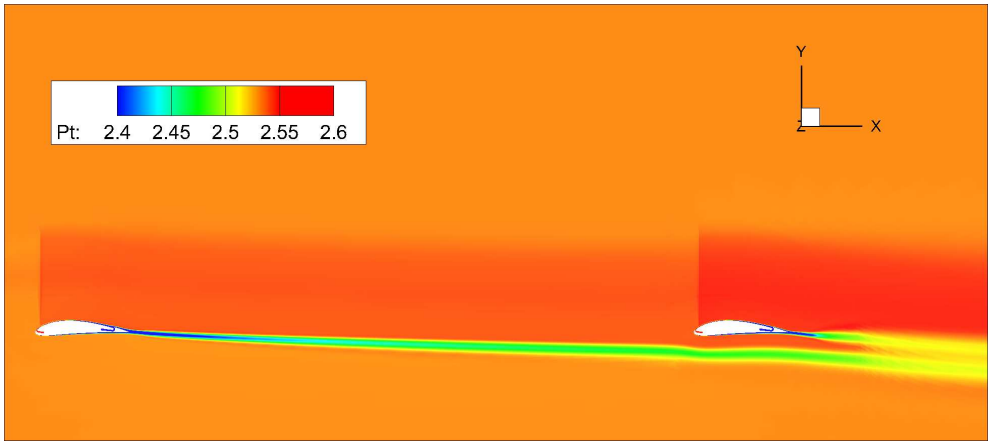

Figure 10. Mid-span total pressure contours of the tandem wing system with the small wing in the front.

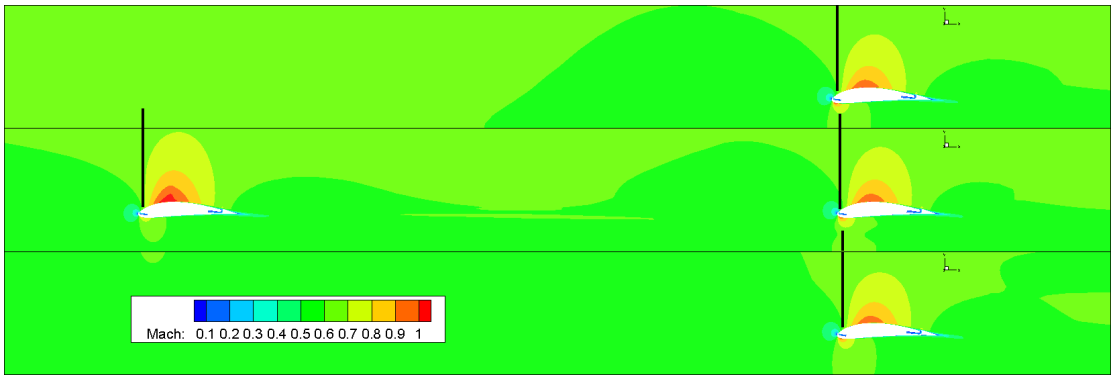

Figure 11. Tandem wing vertical distance trade study with the first wing fixed.

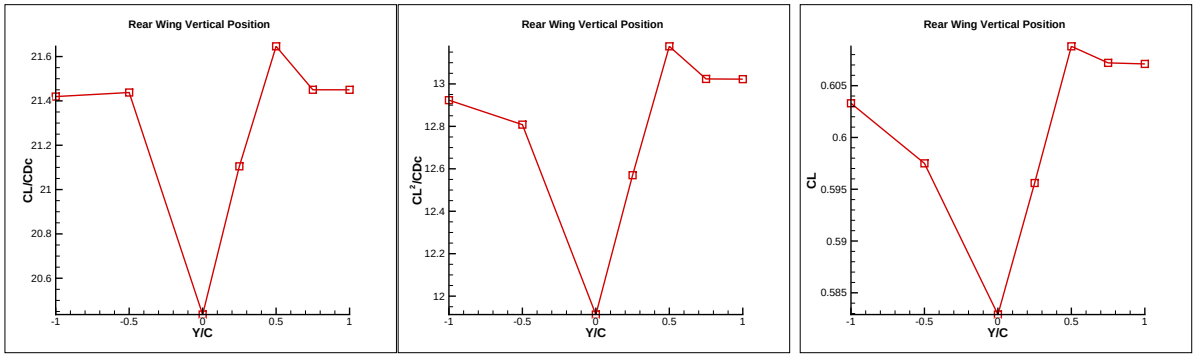

Figure 12. System aerodynamic performance with variation of the vertical location of the large rear wing

This is because that the rear wing is affected by the wake of the front wing and its wing tip vortex as shown in Fig. 9. Translating the rear wing up by $+0.5C$ vertically achieves the optimum efficiency.

Figure 13 shows a spanwise slice of the vertical component of velocity right before the rear wing with the rear wing translated $+0.5C$ vertically. The rear wing avoids most of the downward component of velocity induced by the first wing's wingtip vortex, but is in a large portion of the upwash of the front wing. This interactions appears to be providing a slight enhancement to the lift and efficiency of the second wing. The interaction between the first and second wing can be also seen in Figure 14, which is the isentropic Mach number distribution on the wing surface for the rear wing translated $+0.5c$ vertically. The plot on the left in Figure 14 is the mid-span result of the single wing simulation at the same freestream condition at an incidence angle of 0°, which provides the optimum efficiency for the single wing. The plot on the right of Figure 14 are the results at different span of the rear wing. The isentropic Mach number distribution indicates that the inner span of the wing sees significantly reduced effective incidence angle due to the

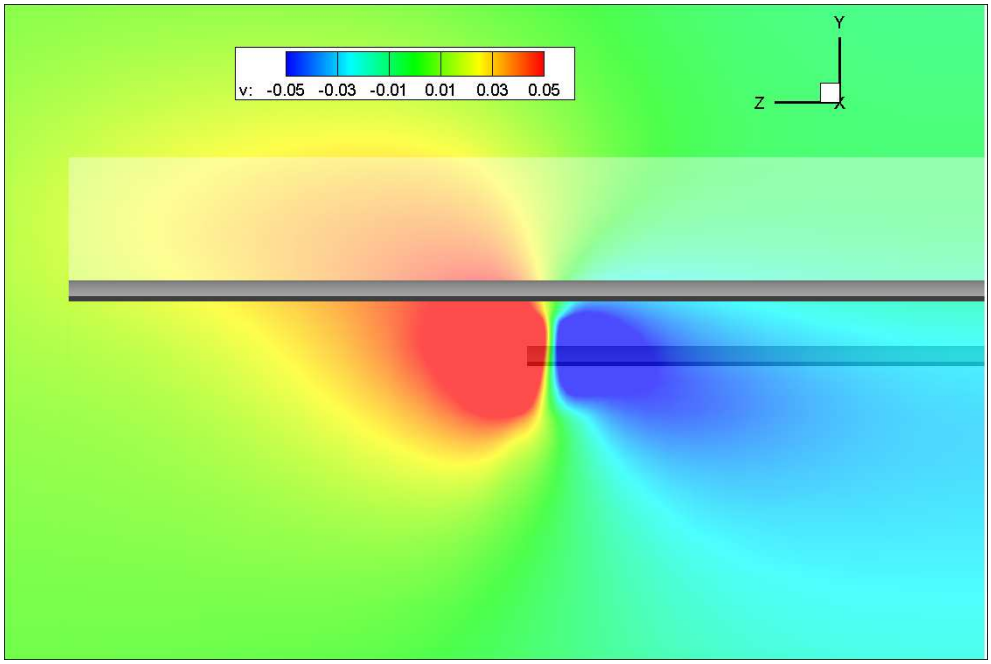

Figure 13. Vertical velocity contours showing the small front wing tip vortex effect on the large rear wing at position Y=+0.5C

downwash of the front wing. The rear wing is exactly twice as long as the front wing in span. The outer span of the rear wing is not affected much by the front wing. The flow interaction of the inner-span clearly hurts the overall performance.

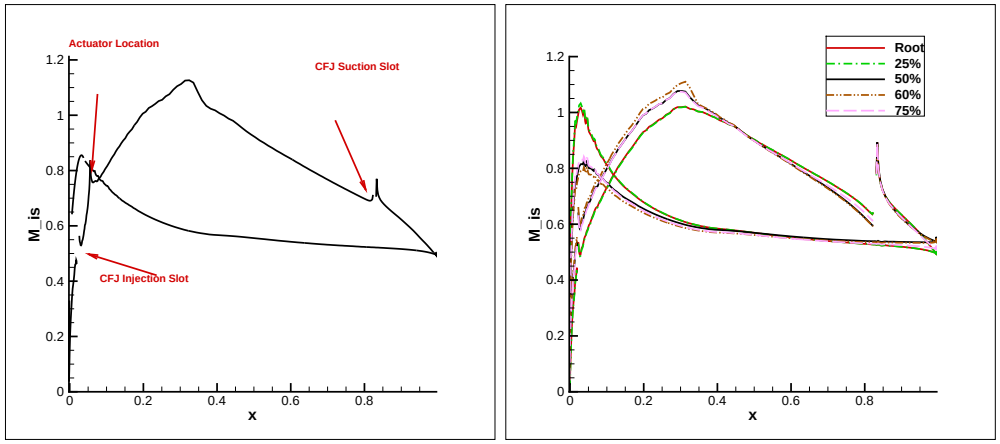

Figure 14. Surface isentropic Mach number distribution: (A) Single Wing mid-span, (B) Rear Wing at various span locations, y=+0.5c

III.B.2. Front Wing AR14, Rear Wing AR7

To avoid the front wing tip vortex effect, the study then places the larger wing in the front. Since the larger wing provides most of the lift, it is beneficial to have favorable flow conditions for it. The horizontal distance between the two wings remains 7C. The isentropic Mach number contours on the surface in Figure 15 show a relatively uniform freestream flow for both front and rear wings. The wingtip vortex of the lead wing does not interfere with the rear wing because the wing span of the front wing is larger. The efficiency of the small rear wing is decreased compared with the case that the small wing is in the front in Section III.B.1 due to the downwash, but has smaller impact on the overall system efficiency since the planform area of the second wing is only 50% of the front wing. This can be seen in the vertical distance trade study in Figure 16.

As with the previous trade study, the small rear wing vertical position is varied for this new trade

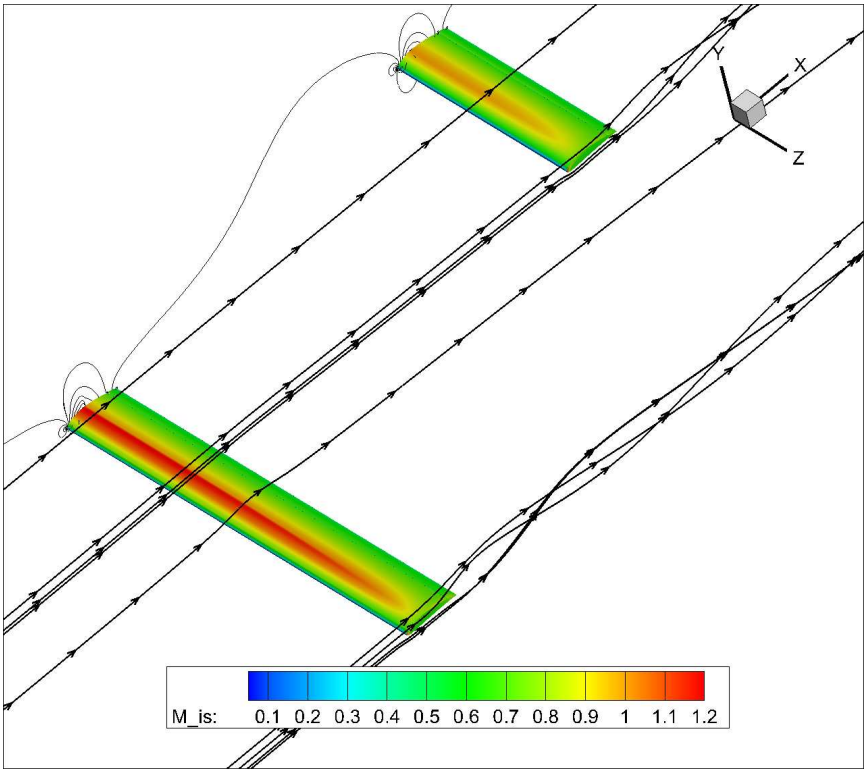

Figure 15. Tandem wing Mach number contours with streamlines, large wing in the front, small wing in the rear.

study. Consistent with the previous section, the rear wing located directly in the wake of the first wing gives the worst performance. Moving the rear wing vertically upward or downward has nearly symmetrical performance benefits. There is little upwash benefit as with the small wing in the front because the tip vortex is further away spanwise. The trade study shows that the further away the rear wing is placed vertically, the more efficient the system due to less interaction of the front wing. The final vertical position for the rear wing is at 1.5C above the front wing, which is constrained by the fuselage size. The optimum system efficiency putting the large wing in the front is about 5% better than putting it in the rear as in Section III.B.1. To compensate the down wash created by the front wing, a trade study is done to increase the incidence angle of the small rear wing and the results are shown in Figure 16, which indicates that increasing the rear wing's incidence angle hurts its efficiency as quantified in Table 3. The trade study to vary the axial distance shows that the system is not sensitive to the axial distance as indicated in Fig. 17.

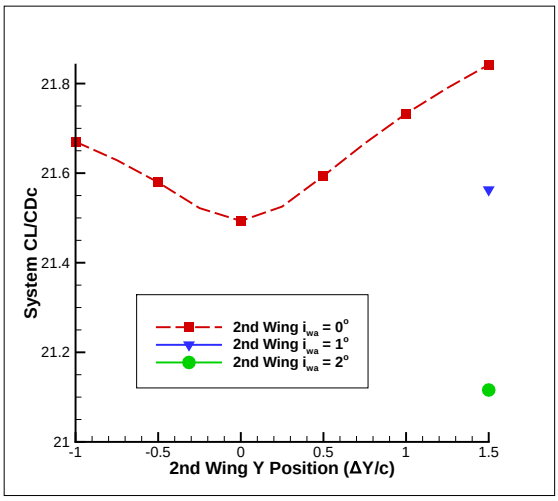

Figure 16. System $C_L/(C_D)_c$ vs small rear wing vertical location.

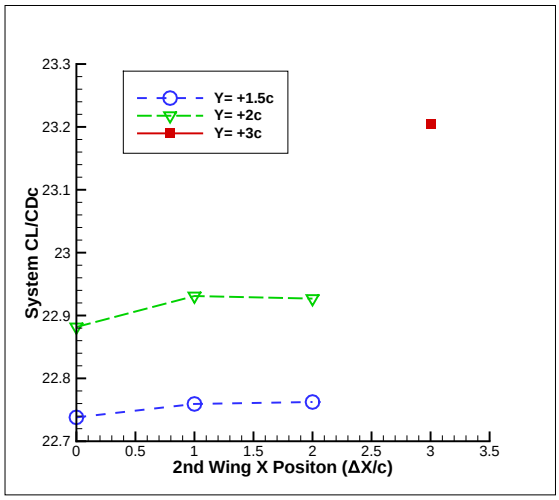

Figure 17. $C_L/(C_D)_c$ vs small rear wing horizontal location, X=7C + Δ X/C

Figure 18 shows the isentropic Mach number distribution of both the front and rear wings at various spanwise locations. These plots contrast with the previous configuration as the lift distribution is relatively constant along the entire span. There is no jump at mid-span since the front wing tip vortex is far beyond the rear wing span. The isentropic Mach distribution is plotted with the first wing at 0.5° incidence angle since it gives the slightly better efficiency than $i_{wf} = 0°$. The results for this slight change of the front wing's incidence angle is summarized in Tables 3 and 4.

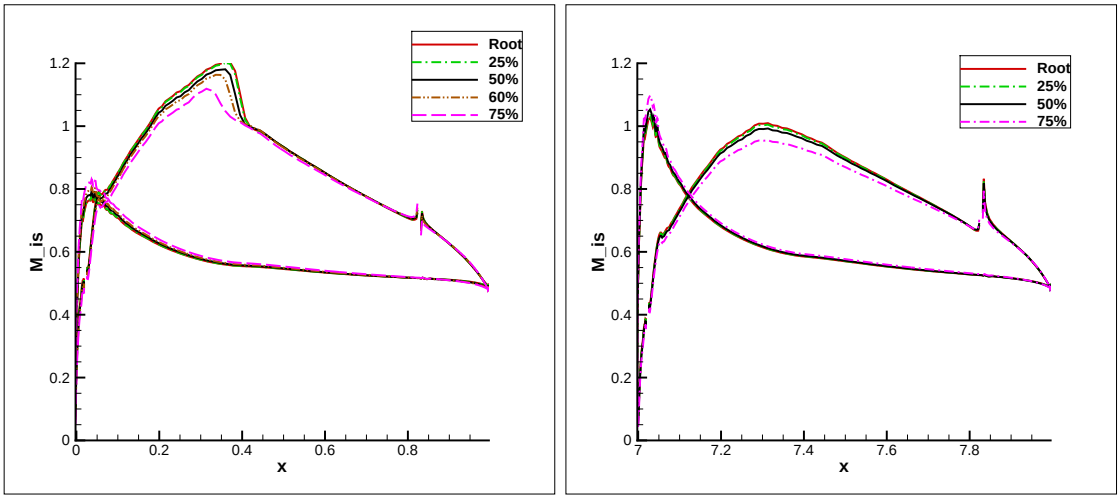

Figure 18. Isentropic Mach number distributions along wing span. Left: front large wing at $i_{wf} = 0.5°$ M_{is}; Right: rear small wing at y=+1.5c position.

Table 3 shows the effect of changing the incidence angle (i_{wa}) of the rear wing. It can be seen that the overall lift coefficient is increased, so is the overall drag coefficient. The increase in drag coefficient outweighs the growth in lift coefficient, which ultimately hurts the overall aerodynamic efficiency, but the productivity efficiency is increased due to a larger lift coefficient.

Table 3. Aerodynamic parameters with front large wing at $i_{wf} = 0°$ and small rear wing at Y+1.5c position.

2nd Wing AoA	Total C_L	Total C_D	Total Pc	Total C_L/C_D	Total $C_L/(C_D)_c$	Total $C_L^2/(C_D)_c$
0	0.672	0.023	0.0065	29.19	22.75	15.30
1	0.705	0.025	0.0064	27.99	22.29	15.73
2	0.739	0.027	0.0063	26.568	21.62	15.999

Table 4. Aerodynamic parameters with front large wing at $i_{wf} = 0.5°$ and small rear wing at $i_{wa} = 0°$ at position Y+1.5c.

	C_L	C_D	Pc	C_L/C_D	$C_L/(C_D)_c$	$C_L^2/(C_D)_c$
1st Wing	0.8167	0.0215	0.0063	37.9076	29.3670	23.9846
2nd Wing	0.4875	0.0306	0.0068	15.9086	13.0175	6.3466
Overall	0.7070	0.0246	0.0064	28.7643	22.7880	16.1110

Keeping $i_{wa} = 0°$ for the second wing and increasing the front wing to $i_{wf} = 0.5°$ obtains a slight increase of aerodynamic efficiency to 22.78 compared with $i_{wf} = 0°$. as shown in Table 4. The productivity efficiency of the system is 16.11. The aerodynamic efficiency of the front wing is 29.37, while the second wing is 13.02. This shows how much the larger wing in the front benefits the system over the smaller wing.

III.C. 3D VTOL Hovering

Using the final tandem wing configuration from the cruise performance trade study in the previous section, a 3D hovering flow at static condition is simulated. The wings are spaced 8 chord lengths horizontally, and 1.5 chord lengths vertically as optimized for cruise condition. The injection slot size is 1.2%, with a C_μ of

1.0. The pressure rise over the propeller actuator is kept from the 2D case at 0.04. The design criterion is that the hovering lift to gross weight ratio $L/W \geq 1.18$.[49] The hovering configuration, including the wing incidence angle and propeller actuator strength, are based on the 2D simulation conducted first. The wings are tilted 80°.

Fig. 19 is 3D Mach contours showing the tandem wings system with the rectangular propellers mounted on the top surface of each wing. The flow is induced downward and rearward by the two rows of propellers toward the wings. The flow hits the ground, forms a stagnation area, and is split into two streams going upstream and downstream on the ground surface. The stream flowing downstream from the front wing encounters the stream flowing upstream of the rear wing. The flow then rolls up from the ground and forms a large vortex in front of the rear wing. A shear layer is formed upstream of the rear wing between the flow rolling up and the flow pulled down from the rear wing. Since the rear wing span is only half of the one of the front wing, the flow hitting ground from the front wing outer span does not roll up, but continues to flow downstream on the ground.

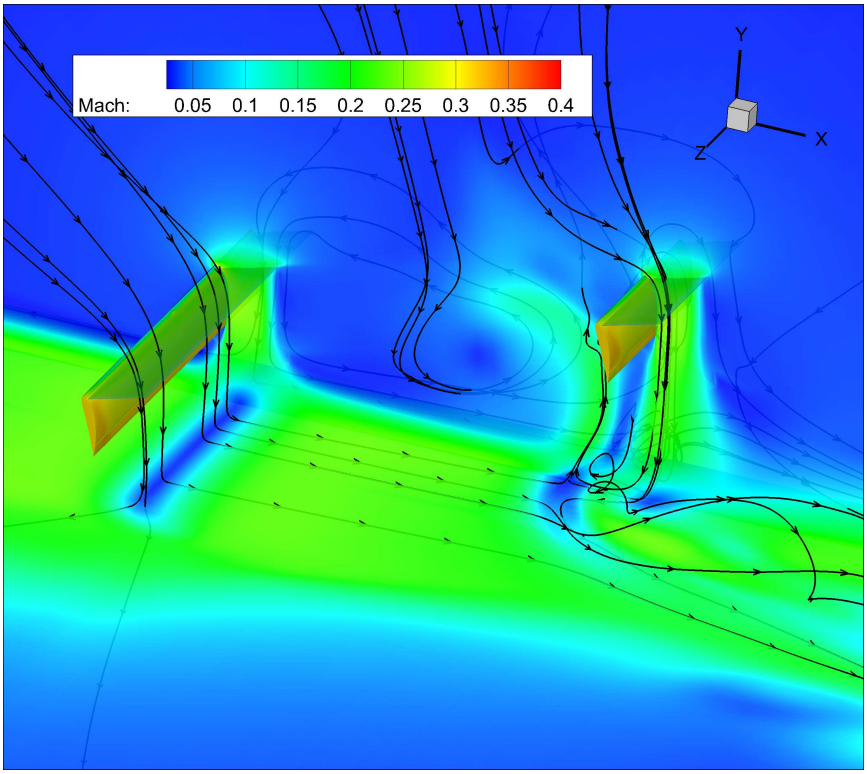

Figure 19. Mach number contours with the streamlines of the tandem wings at hovering condition.

The performance of the 3D CFJ-VTOL hovering system is listed in Table 5. The hovering lift to gross weight ratio achieved is 1.19, which enables the vehicle to vertically takeoff and land with sufficient acceleration. Table 5 indicates that the CFJ wings generate 19% of the total lift, but consume only 1.5% of the total hovering power. This substantially reduces the disk loading and potentially its associated noise. This lift contribution of the wing reduces the disk loading by 16% should all the lift be generated by the propellers. As a result, the system hovering power is decreased by 21.7%, which will reduce the propulsion system weight for the same percentage assuming the propulsion system power density is the same. This will significantly benefit the whole mission efficiency.

The predicted 3D total lift coefficient of the system given in Table 5 is within 2% of the 2D result also listed in the same Table. All other component results are on the similar order of variation between the 2D and 3D simulation. The high solution similarity between 2D and 3D simulation for hovering condition is substantially smaller than the situation when there is incoming freestream flow. This appears to be attributed to the static ambient condition that does not have much dynamic pressure effect.

The Mach number contours with the streamlines of the instantaneous flow-field are visualized in Figures 20, 21, 22, and 23 at span location of 5%, 25%, 45% and 90% based on the front larger wing. Since the front wing has twice the span of the rear wing, the flow-field position is listed as a percentage of both spans. For instance, the 25% span of the front wing is at the 50% span of the rear wing. Attached beneath

Table 5. 3D CFJ-NACA 6415 Tandem Wing and 2D CFJ-NACA-6415-2D Tandem Airfoil Systems Performance at Hovering

Parameter	2D	3D
C_μ	1.0	1.0
C_{LCFJ}	8.65	9.75
C_{DCFJ}	10.48	10.09
Pc_{CFJ}	0.300	2.186
C_{Lprop}	41.69	41.50
C_{Dprop}	-11.48	-11.61
Pc_{prop}	142.2	141.48
C_{Ltot}	50.34	51.26
C_{Dtot}	-0.998	-1.521
Pc_{tot}	142.5	143.6
$D_L(lb/ft^2)$	103.59	103.25
$P_L(HP/1000lb)$	233.75	231.45
$P_{L_{Proponly}}(HP/1000lb)$	292.98	295.63
$\Delta P_L\%$	-20.2%	-21.7%

each Mach number contours are the isentropic Mach number distributions on the wing surface at the same span location. The flow structures are the same as those observed in Fig. 19. As shown in Fig. 20 and 21 at 5% and 25% span of the front wing, the stream from the front wing on the ground rolls up and forms a shear layer in front of the rear wing. At the span of 45% of the front wing that is 90% span of the rear wing as shown in Fig. 22, the ground stream of the front wing only rolls up slightly, merges with the tip flow of the rear wing and flows downstream. At the span of 90% of the front wing, where the rear wing blockage does not exist as shown in Fig. 22, the ground stream of the front wing does not roll up at all and flows along the ground wall downstream. For both the front and rear wing, the isentropic Mach number distributions indicate that the wings are highly loaded with very high incidence angle. The peak Mach number at the wing leading edge is close to 0.5 at the incidence angle of 80°, indicating a very strong leading suction effect at the static hovering condition for an ultra-high lift coefficient. The injection Mach number is about 0.3 or lower for both the front and rear wing. The low injection Mach number is desirable to keep the noise level low and the CFJ system efficient. Comparing the results from the 5% span to the 90%, even though the flow field is chaotic, the isentropic Mach distribution is similar across the entire wing span of the front wing, indicating the 3D effect is not severe until reaching the tip. The rear wing suffers some flow separation at 90% span as shown by the Mach contours and the surface isentropic Mach number distribution in Figure 22. Comparing this result with the 90% span of the front wing in Figure 23, the front wing's outer span has the flow very well attached because it has little interference from the rear wing.

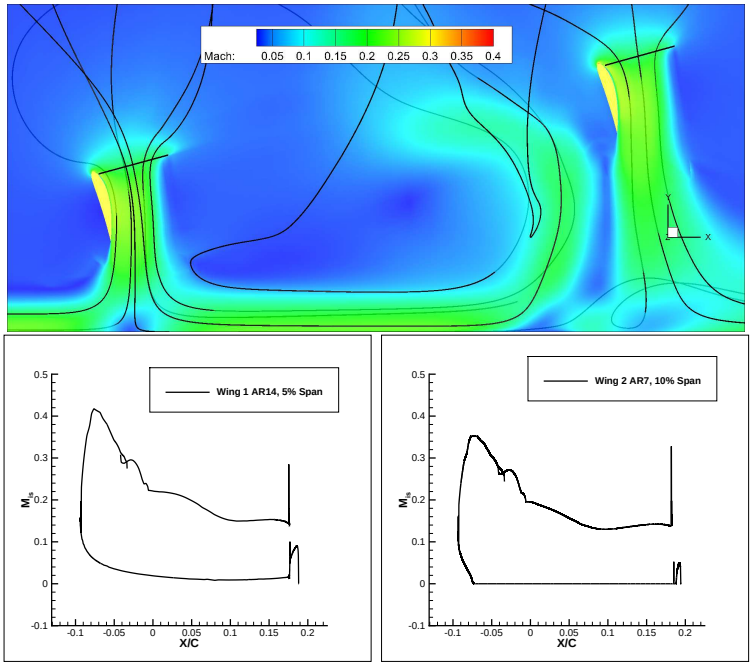

Figure 20. Mach contours and Isentropic Mach Distribution of Front and Rear wings at 5% span of Front wing.

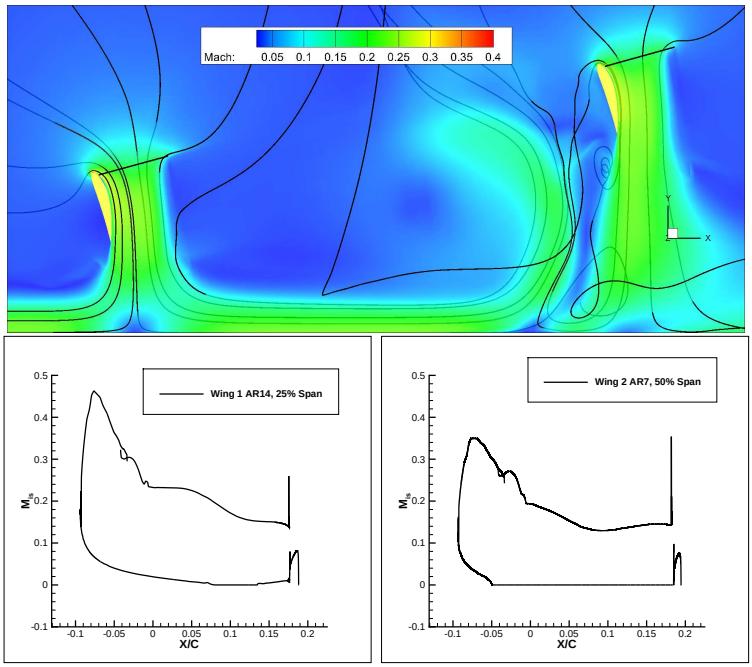

Figure 21. Mach contours and Isentropic Mach Distribution of Front and Rear wings at 25% span of Front wing.

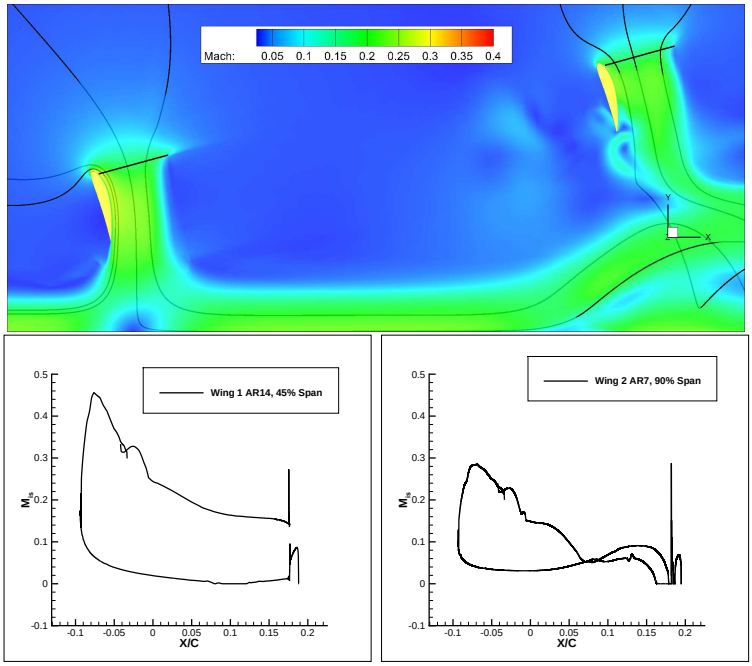

Figure 22. Mach contours and Isentropic Mach Distribution of Front and Rear wings. 45% span of Front wing.

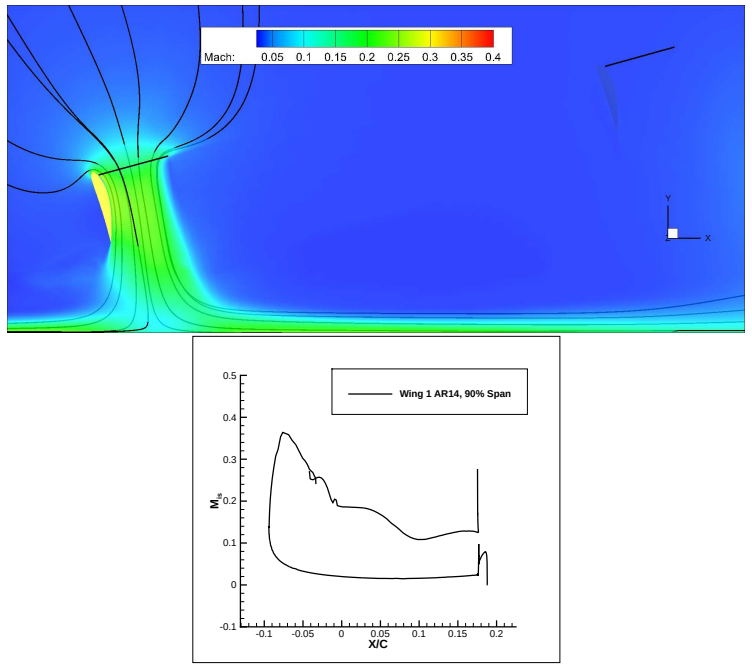

Figure 23. Mach contours and Isentropic Mach Distribution of Front and Rear wings at 90% span of Front wing.

In designing the full aircraft at cruise condition, the trimmed Center of Gravity (CG) is located at 1.35 chord downstream of the trailing edge of the large front wing. In the VTOL hovering, there is slight nose-up pitching moment. Such a small mismatch can be controlled by increasing the actuator strength of the rear wing about 10%.

III.D. Full Aircraft Simulation at Cruise

The whole aircraft with fuselage, tandem wings and propeller actuators, similar to the configuration in Fig. 5, is simulated at cruise condition as shown in Fig. 24. The fuselage is sized for 1500 kg payload or 15

passenger seats with the volume for propulsion and energy storage (e.g. fuel, batteries, motors, generators, etc). The rear wing is separated from the front wing by 8 chords axial length and 1.5 chords vertical length, which is based on the previous tandem wing trade study. The front wing has an incidence of 0.5° with the area and span twice larger and the rear wing has an incidence of 0°.

Fig. 24 displays the surface isentropic Mach number contours with streamlines and vorticity contours. The propellers are shown as the translucent rectangle disks. The surface isentropic Mach numbers contours show that the flow forms a supersonic region on the suction surface of both the wings, with the front wing having high Mach number with more load. The high speed region on the front part of the fuselage contributes the lift generated by the fuselage. The vorticity contours demonstrate the wake and tip vortex of each wing propagating downstream. It can be seen that the front wing tip vortex is far away from the rear wing. The vortices of the two wings have little interaction. However, the rear wing is largely affected by the downwash of the front wing as will be seen below.

Table 6 gives the aerodynamic performance parameters of the aircraft at cruise. In the tandem wing study without the fuselage, the lift coefficient is 0.707. The fuselage contributes some lift and increase the whole aircraft lift coefficient by 14.8% to 0.812. However, the fuselage increases the drag coefficient by 81% to 0.0491.

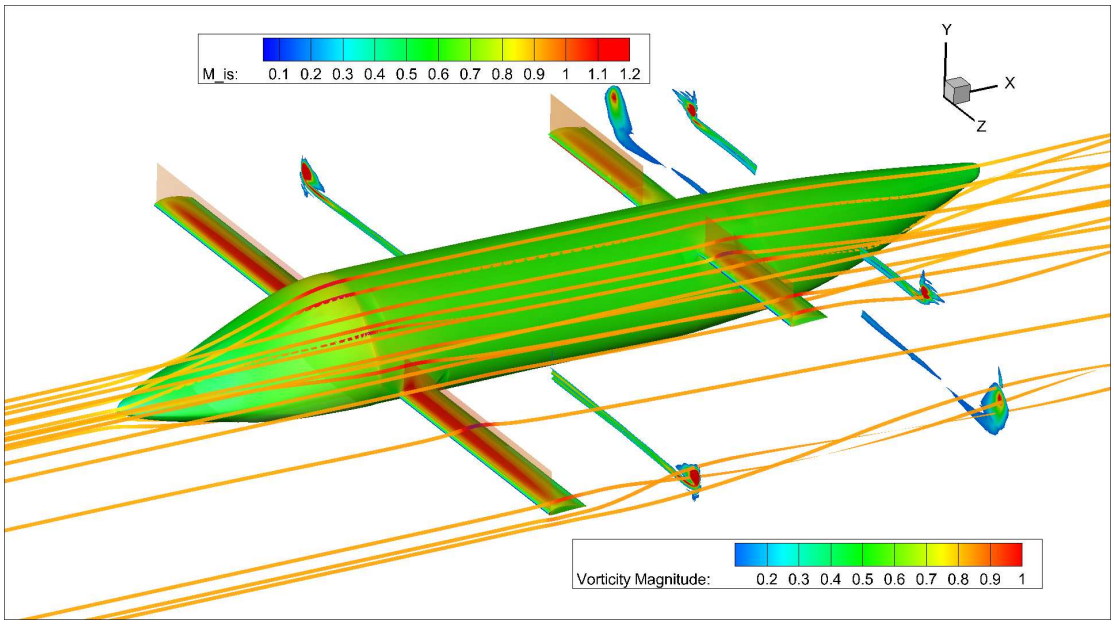

Figure 24. Mach number contours and streamlines of the full tandem wings aircraft at cruise.

Table 6. Aerodynamic parameters of the full aircraft simulation.

	C_L	C_D	P_c	C_L/C_D	$(C_L/C_D)_c$	$C_L^2/(C_D)_c$
Fuselage	0.166	0.0220	-	-	-	-
Total CFJ Wings	0.646	0.0271	0.0064	23.85	19.30	12.47
Front Wing	0.844	0.026	0.0063	32.44	26.09	22.08
Rear Wing	0.251	0.030	0.0065	8.56	7.00	1.76
Full Aircraft	0.812	0.0491	0.0064	16.55	14.63	11.89

Figure 25 shows the isentropic Mach number distribution at mid-span of both the front and rear wings. This is similar to Figure 18, which is the isentropic Mach number distribution of the tandem wings without the fuselage. Compared with Fig. 18, it is observed that the front wing shock wave becomes slightly stronger, which increases front wing lift coefficient by 3.3% from 0.817 (see Table 4) to 0.844. The drag of the front wing due mostly to the wave drag is increased by 21% from 0.0215 to 0.026. The other difference observed from the plot on the right in Figure 25 is that the rear wing sees more downwash with smaller incidence angle than the result with no fuselage shown in Fig. 18. The stronger downwash reduces the lift coefficient of the rear wing by 48.5% from 0.4875 to 0.251. Fig. 26 is the Mach number contours with

streamlines at mid-span of the front wing for the full aircraft simulation. It shows that the front wing has a stronger shock wave with higher loading and the rear wing is less loaded.

Overall, the 3D tandem wing aircraft configuration is a preliminary geometry to demonstrate the concept without any blending between the wings and the fuselage. No systematic design optimization is conducted for this configuration. Even so, Table 6 indicates that the corrected aerodynamic efficiency is 14.63. This is substantially higher than the L/D of 9 for the SoA of VTOL aircraft as shown in Fig. 2.

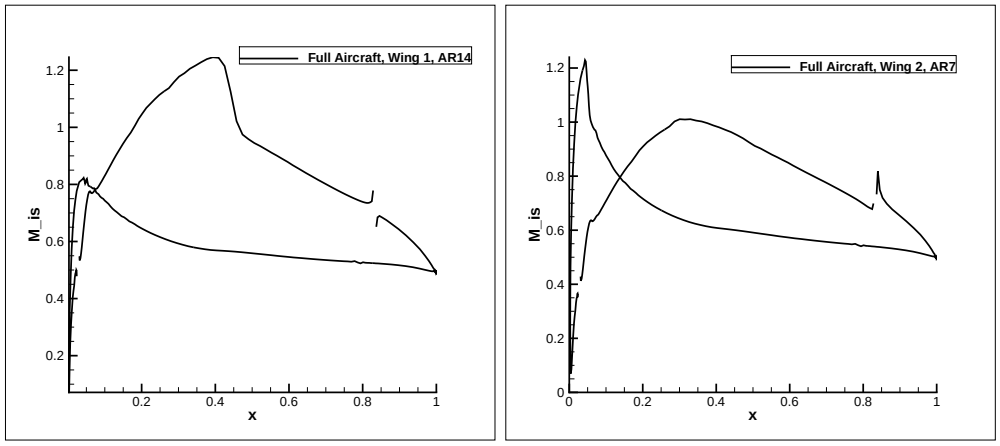

Figure 25. Surface isentropic Mach number distribution, Left: large front wing at mid-span at $i_{wf} = 0.5^\circ$ M_{is}; Right: small rear wing at mid-span at y=+1.5c.

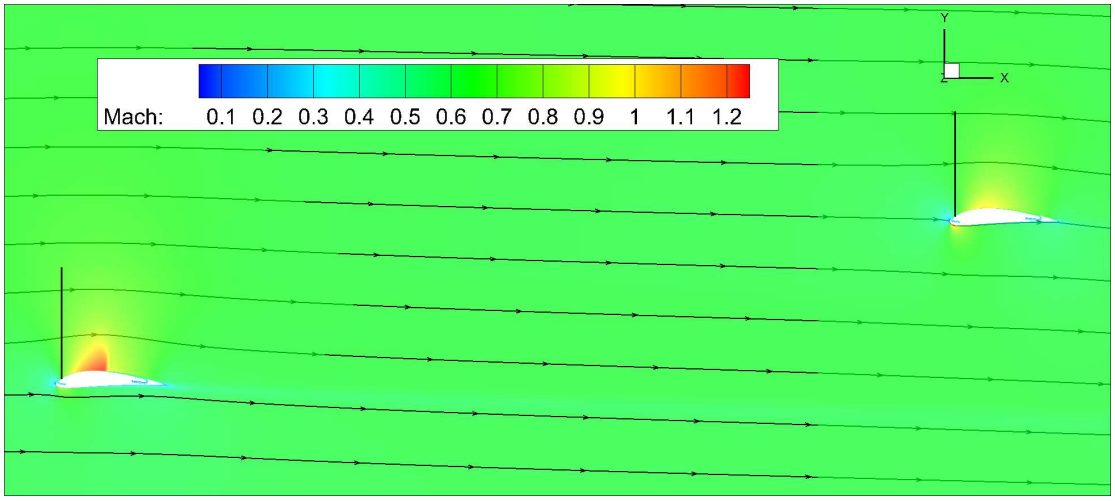

Figure 26. Mach number contours with streamlines at 25% of the front wing for the full aircraft simulation.

III.E. Comparison with the SoA VTOL Aircraft

The conceptual design of the high speed CFJ-VTOL aircraft indicates that the concept is promising to achieve excellent mission efficiency. Table 7 lists the comparison of the SoA VTOL with the conceptual CFJ-VTOL aerodynamic design conducted in this paper. The SoA aircraft performance data are the highest values from the existing VTOL aircraft that are made. For example, the Mach number of 0.42 is from V-280 representing the fastest VTOL aircraft today. The cruise lift coefficient C_L of 0.6 is based on the statistics of subsonic fixed wing aircraft with the maximum efficiency. The aerodynamic efficiency C_L/C_D of 9 is the highest value from Fig. 2 based on the AHS/NARI 2018 report.[3] No conceptual designs conducted by any other groups that may have advanced performance are included in Table 7 to avoid comparison uncertainty.

Table 7 also only intends to list the designed aerodynamic performance for VTOL aircraft instead of the actual performance to avoid the uncertainty for comparison. The actual performance depends on the manufacturing techniques that can vary among manufacturers. For example, the designed aerodynamic efficiency $C_L/C_D = L/D$ implies that the required power $P_{req} = DV_\infty$. But the actual power used is

$P_{act} = DV_\infty/\eta$, where η is the propeller efficiency and can vary for different manufacturers. Even for the same C_L, or C_D, or η, different manufacturers may have different technologies to achieve them with different weights, which affect the ultimate performance and efficiency of the aircraft. For the same reason, the figure of merit (FM) is not used in Table 7 to compare the hovering efficiency because FM depends the actual process. Instead, a normalized hovering power loading or power coefficient that depends on the same ratio of (gross weight)/(propeller area) is used for comparison. In other words, Table 7 lists the performance improvement that CFJ-VTOL can achieve in principle.

Table 7 lists all the SoA aircraft aerodynamic performance data together and assumes that they occur for the same vehicle. In reality, they do not occur together. For example, the highest cruise Mach number of 0.42 is from V-280, which will not have the highest C_L/C_D of 9 at the same time. Actually, according to Datta and Ng,[3,50] the peak C_L/C_D of 9 occurs at Mach number of about 0.22. For cruise Mach number higher than that, the C_L/C_D of SoA VTOL continuously decreases. Hence the comparisons in Table 7 are on the conservative side since all the CFJ-VTOL performance do occur for the same vehicle.

Table 7. Comparison of the high speed CFJ-VTOL with the SoA VTOL Aircraft

Performance	SoA VTOL	CFJ-VTOL	Improvement
Mach	0.42	0.6	43%
C_L, cruise	0.6	0.812	35%
P_L, hovering at same (gross weight)/(disk area)	1	0.773	21.7%
$(C_L/C_D)c$, cruise	9	14.6	62%
$(C_L^2/C_D)c$, cruise	5.4	11.86	119%

Table 7 indicates that the CFJ-VTOL vehicle cruising at Mach number of 0.6 would be 43% faster than the SoA. The Mach number of 0.6 chosen for this study is just an example to demonstrate the concept. It is not the limit. The limit would be the typical limit for propeller cruise efficiency up to Mach 0.8. In the case of cruising Mach numbers greater than 0.6, a super-critical airfoil may be necessary. The propeller interaction with the supersonic flow needs to be avoided.

For the same aircraft gross weight, the over 20% reduced hovering power shown in Table 7 can reduce the same percentage of the propulsion system weight assuming the propulsion systems have the same power density. The saved weight can be used for more payload or more energy storage for longer range. This would be a very substantial benefit for the mission efficiency.

At cruise, the aerodynamic efficiency $(C_L/C_D)c$ is 62% higher than the SOA. More importantly, the productivity efficiency $(C_L^2/C_D)c$ is 119% higher. That means if the aircraft have the same gross weight, the CFJ-VTOL would have 119% longer range. Conversely, for the same range the CFJ-VTOL would have 119% more gross weight to increase payload.

Based on the hovering power reduction and cruise productivity efficiency improvement compared with the SoA VTOL aircraft, a 100% improvement of the overall mission productivity appears to be achievable in principle. Furthermore, the same aircraft can be used for ESTOL to save more energy if there is any space to be used as a runway. This study presents a promising goal to advance VTOL to high speed transonic regime with high efficiency. However, achieving the target requires substantial research and technology development. In particular, the CFJ technology is new and is not mature. The encouraging thing is that the CFJ has low energy expenditure and the micro-compressors actually achieve efficiency as high as 80%,[18] the same efficiency level as propellers. Furthermore, the micro-compressors have higher power density than propellers due to its very high RPM (e.g. 140k). We see no technology barriers that can not be overcome, but there are some technology gaps that need more research and development to address.

IV. Conclusions

The conceptual aerodynamic design of the high speed CFJ-VTOL vehicle with detailed 3D CFD simulation is shown to achieve high mission efficiency at cruise Mach number of 0.6. The aircraft has a tandem wing tailless configuration with the fuselage designed for 1.5 ton payload or 15 passenger seats. The overall aspect ratio of the tandem wing system is 11.65. The wing has no sweep and taper and is formed by CFJ-NACA6415 airfoil. The CFJ-NACA6415 airfoil outperforms the supercritical NASA-SC(2) 0714 airfoil to accommodate the propeller position for the CFJ-VTOL configuration, which has the propeller

located near leading edge downstream of the CFJ injection slot. The high camber of the CFJ-NACA6415 airfoil keeps the supersonic flow in the mid-chord region so that the propeller can operate in subsonic flow area, which provides a high efficiency for both the propeller and the airfoil. A trade study is conducted to investigate the tandem wing system, which positions the large wing with an aspect ratio of 14 in the front and the smaller wing with 50% smaller area and wing span aft. Such a configuration has better aerodynamic efficiency than the one with the smaller wing in the front and minimizes the front wing tip vortices and downwash interference to the rear wing. When the smaller wing is in the front, the large rear wing positioned at 0.5C above the front wing has the optimum efficiency and benefited from the front wing upwash effect. When the large wing is in the front, the further apart of the rear wing vertically, the more efficient of the wing system due to the mitigated effect of the front wing. The small rear wing has similar effect located above or below the front wing since the tip vortex effect is far beyond the span. Overall, the tandem wings are not very sensitive to the horizontal distance between the two wings regardless which wing is in the front.

At cruise, the full aircraft with the fuselage and the tandem wing system achieves a very good aerodynamic efficiency $(C_L/C_D)_c$ of 14.6, which includes the CFJ power. Compared with the tandem wing system only at the cruise condition, the fuselage contributes some lift and increases the whole aircraft lift coefficient by 14.8% to 0.812. However, it increases the drag coefficient by 81%. The fuselage negatively impacts the rear wing significantly more the front wing at cruise. At hovering static condition, the CFJ wing is positioned at an incidence angle of 80° that keeps the flow attached and generates high lift making use of the flow pulled by the propeller. The hovering lift to weight ratio L/W is 1.19. The CFJ wings generate 19% of the total lift, but consume only 1.5% of the total hovering power. This substantially reduces the disk loading and potentially its associated noise. As a result, the system hovering power is decreased by 21.7%, which reduces the propulsion system weight by the same amount percentage assuming the same propulsion system power density. The reduced weight will significantly benefit the whole mission efficiency. The peak Mach number at the wing leading edge is close to 0.5 at the hovering condition with the wing incidence angle of 80°, indicating a very strong leading suction effect for ultra-high lift coefficient. The injection Mach number is about 0.3 or lower for both the front and rear wing. The low injection Mach number is desirable to keep the noise level low and the CFJ system efficient. The propellers on the 3D wing are simulated by a rectangle actuator disk to mimic distributed propulsors. In reality, the rectangle propeller effect may be obtained by overlapping the propeller blades. The conceptual aerodynamic design with high fidelity CFD simulation indicates that the CFJ-VTOL concept is not just feasible for cruise at Mach number 0.6 and higher in transonic regime, it is also possible to increase the mission productivity efficiency substantially (e.g. by 100% or higher) compared to the State of the Art conventional VTOL aircraft. We see no technology barriers that can not be overcome, but there are some technology gaps that need more research and development to address.

V. Future Work

This conceptual aerodynamic design and trade study open up more avenues to future VTOL configurations. The initial study is focused mainly on hovering and cruise aerodynamic performance. The fuselage needs more refinement to further reduce drag. More realistic, circular actuator discs will also be used in future work. The stability and flight control need to be studied. This opens up the following future studies:

1. Fuselage Optimization
2. Longitudinal Static Stability Study
3. Roll, Pitch and Yaw Control
4. Circular propellers interaction with the CFJ Wing

VI. Acknowledgments

The simulations are conducted on Pegasus supercomputing system at the Center for Computational Sciences at the University of Miami. The work is partially supported by the 2019 AFOSR Summer Faculty Fellowship Program. The Dean's Fellowship for graduate students and the teaching assistantship from the University of Miami are appreciated.

This paper has been reviewed and cleared for public release by the United States Air Force (Case Number: 88ABW-2020-1573).

Disclosure: The University of Miami and Dr. Gecheng Zha may receive royalties for future commercialization of the intellectual property used in this study.

References

[1] H. D. Kim, A. T. Perry, and P. Ansell. A Review of Distributed Electric Propulsion Concepts for Air Vehicle Technology. AIAA 2018-4998, 2018 AIAA Propulsion and Energy Forum, 2018 AIAA/IEEE Electric Aircraft Technologies Symposium, Cincinnati, Ohio, July 9-11, 2018.

[2] H. D. Kim, J. J. Berton, and S. M. Jones. Low noise cruise efficient short take-off and landing transport vehicle study. AIAA 2006-7738, 6th AIAA Aviation Technology, Integration and Operations Conference (ATIO), Wichita, Kansas, Sept. 25-27, 2006.

[3] AHS and NARI. COMMERCIAL INTRA-CITY ON-DEMAND ELECTRIC-VTOL STATUS OF TECHNOLOGY. AN AHS/NARI TRANSFORMATIVE VERTICAL FLIGHT WORKING GROUP-2 REPORT, edited by E. Datta, Jan 15, 2018.

[4] G.-C. Zha, Y. Ren, J.-Y. Gan, and D. Espinal. A High Efficiency Low Noise VTOL/ESTOL Concept Using CoFLow Jet Airfoil. AIAA Paper 2019-4467, AIAA Propulsion and Energy 2019 Forum, Indianapolis, Indiana, 19-22 August 2019.

[5] Zha, G.-C. and Gao, W. and Paxton, C. Jet Effects on Co-Flow Jet Airfoil Performance. *AIAA Journal, No. 6,*, 45:1222–1231, 2007.

[6] G.-C. Zha and D. C. Paxton. A Novel Flow Control Method for Airfoil Performance Enhancement Using Co-Flow Jet. *Applications of Circulation Control Technologies*, Chapter 10, p. 293-314, Vol. 214, Progress in Astronautics and Aeronautics, AIAA Book Series, Editors: Joslin, R. D. and Jones, G.S., 2006.

[7] Zha, G.-C and Paxton, C. and Conley, A. and Wells, A. and Carroll, B. Effect of Injection Slot Size on High Performance Co-Flow Jet Airfoil. *AIAA Journal of Aircraft*, 43, 2006.

[8] Zha, G.-C and Carroll, B. and Paxton, C. and Conley, A. and Wells, A. High Performance Airfoil with Co-Flow Jet Flow Control. *AIAA Journal*, 45, 2007.

[9] Wang, B.-Y. and Haddoukessouni, B. and Levy, J. and Zha, G.-C. Numerical Investigations of Injection Slot Size Effect on the Performance of Co-Flow Jet Airfoil . *AIAA Journal of Aircraft*, 45:2084–2091, 2008.

[10] B. P. E. Dano, D. Kirk, and G.-C. Zha. Experimental Investigation of Jet Mixing Mechanism of Co-Flow Jet Airfoil. AIAA-2010-4421, (5th AIAA Flow Control Conference, Chicago, IL), 28 Jun - 1 Jul 2010.

[11] B. P. E. Dano, G.-C. Zha, and M. Castillo. Experimental Study of Co-Flow Jet Airfoil Performance Enhancement Using Micro Discreet Jets. AIAA Paper 2011-0941, 49th AIAA Aerospace Sciences Meeting, Orlando, FL,, 4-7 January 2011.

[12] Lefebvre, A. and Dano, B. and Bartow, W. and Di Franzo, M. and Zha, G.-C. Performance and Energy Expenditure of Co-Flow Jet Airfoil with Variation of Mach Number. *AIAA Journal of Aircraft*, 53:1757–1767, 2016.

[13] Lefebvre, A. and Zha, G.-C. Numerical Simulation of Pitching Airfoil Performance Enhancement Using Co-Flow Jet Flow Control. AIAA Paper 2013-2517, AIAA Applied Aerodynamics Conference, San Diego, CA, 24 - 27 June 2013.

[14] Lefebvre, A. and Zha, G.-C. . Design of High Wing Loading Compact Electric Airplane Utilizing Co-Flow Jet Flow Control. AIAA Paper 2015-0772, AIAA SciTech2015: 53rd Aerospace Sciences Meeting, Kissimmee, FL, 5-9 Jan 2015.

[15] Lefebvre, A. and Zha, G.-C. Trade Study of 3D Co-Flow Jet Wing for Cruise and Takeoff/Landing Performance. AIAA Paper 2016-0570, AIAA SCITECH2016, AIAA Aerospace Science Meeting, San Diego, CA, 4-8 January 2016.

[16] Liu, Z.-X. and Zha, G.-C. Transonic Airfoil Performance Enhancement Using Co-Flow Jet Active Flow Control. AIAA Paper 2016-3472, AIAA AVIATION 2016, 8th AIAA Flow Control Conference, Washington, D.C, June 13-17, 2016.

[17] Yang, Y.-C. and Zha, G.-C. Super-Lift Coefficient of Active Flow Control Airfoil: What Is the Limit? AIAA Paper 2017-1693, AIAA SCITECH2017, 55th AIAA Aerospace Science Meeting, Grapevine, Texas, 9-13 January 2017.

[18] G.-C. Zha, Y.-C. Yang, Y. Ren, and B. McBreen. Super-lift and thrusting airfoil of coflow jet-actuated by micro-compressors. AIAA Paper 2017-3061, AIAA AVIATION 2018, Atlanta, GA , 25 - 29 June 2018.

[19] Y. Ren and G.-C. Zha. Design of injection and suction ducts for co-flow jet airfoils with embedded micro-compressor actuator. AIAA Paper 2018-3062, AIAA AVIATION 2018, Atlanta, GA, 25 - 29 June 2018.

[20] Yang, Y.-C. and Zha, G.-C. Conceptual Design of a CoFlow Jet Hybrid Electric Regional Airliner. AIAA Paper 2019-1584, AIAA SciTech 2019 Forum, San Diego, CA, 7-11 January 2019.

[21] Y.-C. Yang. Investigations of super-lifting co-flow jet airfoil and distributed electric propulsion aircraft. Ph.D. Dissertation, University of Miami, Florida, USA, May 2018.

[22] Kewei Xu and Gecheng Zha. Design of high specific speed mixed flow micro-compressor for co-flow jet actuators. ASME Paper GT-2019-90980, ASME IGTI Turbo Expo 2019, Phoenix, Arizona, USA, June 17 - 21, 2019.

[23] Kewei Xu and Gecheng Zha. High Control Authority 3D Aircraft Control Surfaces Using Co-Flow Jet. AIAA Paper 2019-3168, AIAA Aviation 2019, Dallas, Texas, 17-21 June 2019.

[24] Kewei Xu and Gecheng Zha. Drag Minimization of Co-Flow Jet Control Surfaces at Cruise Conditions. AIAA Paper 2019-1848, SciTech 2019, San Diego, CA, USA, 7-11 January 2019.

[25] P Patel and Gecheng Zha. Investigation of mixed micro-compressor casing treatment using non-matching mesh interface. ASME Paper GT-2019-90977, ASME IGTI Turbo Expo 2019, Phoenix, Arizona, USA, June 17 - 21, 2019.

[26] Yang, Y.-C. and Fernandez, M. and Zha, G.-C. Improved Delayed Detached Eddy Simulation of Super-Lift Flow of Co-Flow Jet Airfoil. AIAA Paper 2018-0314, AIAA SciTech Forum, 2018 AIAA Aerospace Sciences Meeting, Kissimmee, FL, 8-12 January 2018.

[27] Y. Ren and G.-C. Zha. Simulation of 3d co-flow jet airfoil with embedded micro-compressor actuator. AIAA Paper 2018-0330, AIAA SciTech Forum, 2018 AIAA Aerospace Sciences Meeting, Kissimmee, FL, 8-12 January 2018.

[28] Y. Wang and G.-C. Zha. Study of 3D Co-flow Jet Wing Induced Drag and Power Consumption at Cruise Conditions. AIAA Paper 2019-0034, AIAA SciTech 2019, San Diego, CA, January 7-11, 2019.

[29] Y. Wang, Y.-C. Yang, and G.-C. Zha. Study of Super-Lift Coefficient of Co-Flow Jet Airfoil and Its Power Consumption. AIAA Paper 2019-3652, AIAA Aviation 2019, AIAA Applied Aerodynamics Conference, Dallas, Texas, 17-21 June 2019.

[30] Y. Wang and G.-C. Zha. Study of Mach Number Effect for 2D Co-Flow Jet Airfoil at Cruise Conditions. AIAA Paper 2019-3169, AIAA Aviation 2019, AIAA Applied Aerodynamics Conference, Dallas, Texas, 17-21 June 2019.

[31] Yang, Y.-C. and Zha, G.-C. Numerical Investigation of Performance Improvement of the Co-Flow Jet Electric Airplane. AIAA Paper 2018-4208, AIAA AVIATION Forum 2018, 2018 Applied Aerodynamics Conference, Atlanta, Georgia, June 25-29, 2018.

[32] A.M.O. Smith. High-Lift Aerodynamics. *Journal of Aircraft*, 12:501–530, 1975.

[33] X. Chen and G.-C. Zha. Implicit Application of Non-Reflective Boundary Conditions for Navier-Stokes Equations in Generalized Coordinates. *International Journal for Numerical Methods in Fluids*, 50, 2006.

[34] Shen, Y.-Q. and Zha, G.-C. and Chen, X.-Y. High Order Conservative Differencing for Viscous Terms and the Application to Vortex-Induced Vibration Flows. *Journal of Computational Physics*, 228(2):8283–8300, 2009.

[35] Y.-Q. Shen and G.-C. Zha. Large Eddy Simulation Using a New Set of Sixth Order Schemes for Compressible Viscous Terms . *Journal of Computational Physics*, 229:8296–8312, 2010.

[36] Shen, Y.-Q. and Zha, G.-C. and Wang, B.-Y. Improvement of Stability and Accuracy of Implicit WENO Scheme. *AIAA Journal*, 47, No. 2:331–344, 2009.

[37] Shen, Y.-Q. and Zha, G.-C. . Improvement of the WENO Scheme Smoothness Estimator. *International Journal for Numerical Methods in Fluids*, 64:DOI:10.1002/fld.2186, 2010.

[38] Shen, Y.-Q. and Zha, G.-C. Improved Seventh-Order WENO Scheme . AIAA Paper 2010-1451, 48th AIAA Aerospace Sciences Meeting, Orlando, FL, Jan. 4-6, 2010.

[39] Y.-Q. Shen and G.-Z. Zha . Generalized finite compact difference scheme for shock/complex flowfield interaction. *Journal of Computational Physics*, doi:10.1016/j.jcp.2011.01.039, 2011.

[40] G.-C. Zha, Y. Shen, and B. Wang. An improved low diffusion E-CUSP upwind scheme . *Journal of Computer & Fluids*, 48:214–220, 2011.

[41] B.-Y. Wang and G.-C. Zha. A General Sub-Domain Boundary Mapping Procedure For Structured Grid CFD Parallel Computation. *AIAA Journal of Aerospace Computing, Information, and Communication*, 5, No.11:2084–2091, 2008.

[42] Im, H.-S. and Zha, G.-C. and Dano, B. P. E. Large Eddy Simulation of Coflow Jet Airfoil at High Angle of Attack. *Journal of Fluid Engineering*, 136(2):021101, 2014.

[43] Wang, B. Y and Zha, G.-C. High Fidelity Simulation of Nonlinear Fluid-Structural Interaction with Transonic Airfoil Limit Cycle Oscillations. *Journal of Fluids and Structures*, doi:10.1016/j.jfluidstructs.2010.02.003, 2010.

[44] B. Van Leer. Towards the Ultimate Conservative Difference Scheme, III. *Journal of Computational Physics*, 23:263–75, 1977.

[45] Im, H-S. and Zha, G-C. Delayed Detached Eddy Simulation of Airfoil Stall Flows Using High Order Schemes . *ASME Journal of Fluids Engineering*, page DOI: 10.1115/1.4027813, 2014.

[46] Wang, B. Y and Zha, G.-C. Detached-Eddy Simulation of a Co-Flow Jet Airfoil at High Angle of Attack. *AIAA Journal of Aircraft*, 48, 5:1495–1502, 2011.

[47] Gan, J.-Y. and Zha, G.-C. Comparison of Drag Prediction Using RANS models and DDES for the DLR-F6 Configuration Using High Order Schemes. AIAA Paper 2016-0553, AIAA SCITECH2016, AIAA Aerospace Science Meeting, San Diego, CA, 4-8 January 2016.

[48] J. Boling, S. Dhakaly, Y.-C. Yang, and G.-C. Zha. Numerical Investigation of Low Speed Performance of Transonic CoFlow Jet Supercritical Airfoil. AIAA Paper 2017-3249, AIAA AVIATION Forum, 35th AIAA Applied Aerodynamics Conference, 5-9 June 2017, Denver, Colorado, 15-19 June, 2020.

[49] Uber Elevate. Fast-forwarding to a future of on-demand urban air transportation. Uber White Paper, Oct. 27, 2016.

[50] W. Ng and A. Datta. Development of Models for Electrochemical Power and Sizing of Electric-VTOL Aircraft . AIAA-Paper 2018-1750, AIAA SciTech Forum, Kissimmee, Florida 2018 AIAA Aerospace Sciences Meeting, 8–12 January 2018.